University of Crete, School of Sciences and Engineering, Department of Physics

Master's Thesis:

Development of a novel photoacoustic imaging prototype for the non-destructive in-depth investigation of cultural heritage items

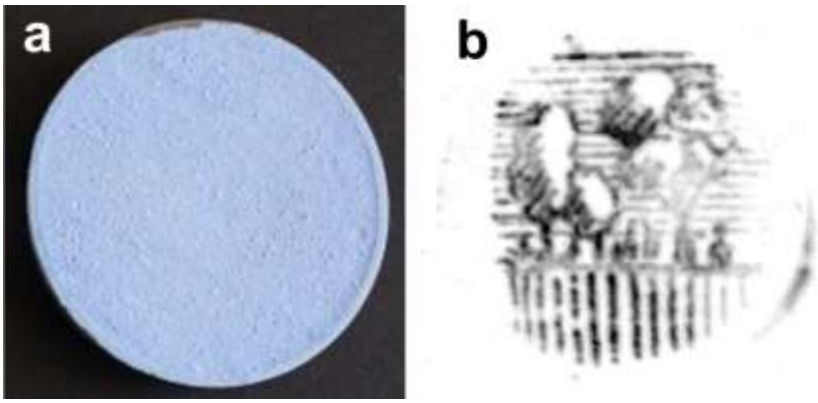

Figure 1: a) Brightfield view of photoacoustic sample coated with acrylic paint.
b) Recovered pattern of the underlying sketch through photoacoustic imaging.

Evgenia Klironomou

Supervisors: K. Makris, G. Zacharakis, D. Charalambidis

Research Associate: G. Tserevelakis

Heraklion, June 2023

FORTH
Foundation for Research & Technology - Hellas

Acknowledgements

My most profound appreciation goes to Prof. Konstantinos Makris, Dr. Giannis Zacharakis and Pr. Dimitrios Charalambidis, the supervisors of this project, for giving me the chance to work with them and deepen my comprehension of the world surrounding us.

The completion of this Master thesis would not have been possible without the guidance and support of Dr. George Tserevelakis, with whom I associated and worked together for nearly three years. The insight he provided me with and the faith he showed in my abilities helped me take initiatives, work passionately and reach the desired goal.

My sincere gratitude also goes to Ms. Kristalia Melessanaki for the preparation of some of the mock-ups used for the needs of this work as well as for the insight she provided me with, concerning the materials and methods used in mural painting. What is more, I would like to thank Dr. Antonina Chaban, Dr. Alice Dal Fovo and Ms. Francesca Assunta Pisu for the fruitful collaborations, the information they shared and the samples they provided us with.

Last but surely not least, I would like to thank my friends and family for the mental support, the encouragement and the faith they showed they have in me. They were the reason why I could complete this project and I am deeply grateful for them.

Table of Contents

1. Introduction

The aim of this work is to enhance the novel, non-destructive imaging prototype based on the photoacoustic imaging (PAI) technique which had been developed during the last couple of years, and is focused on the detection and the imaging of hidden features –e.g. underdrawings– of murals. The capability of detecting underdrawings in works of art has been intriguing for vast the majority of art conservators, as it provides interesting information about an artwork. In PAI, a pulsed laser interacts with the sample, in order to locate and map the spatial distribution of absorbing components, by exploiting the ultrasonic acoustic waves that are being produced. The amplitude of the generated PA waves is proportional to the absorption coefficient of the medium for the employed excitation wavelength. During the past decade, a number of studies have taken place in the area of cultural heritage conservation with modern means, while taking advantage of the technological innovations. In regard to artwork diagnostics, there are many bibliographical references that highlight the importance of such applications for the artistic community.

1.1. The importance of underdrawings

An underdrawing is defined as the initial sketch or drawing made to plan the design of an illustration. An underdrawing can range from extremely detailed drawings to abstract sketches. In some works of art, the underdrawing might be entirely absent. During the time of their creation, the artists could not imagine that underdrawings were going to present any interest, thus they are typically hidden beneath the paint layers in fully painted and finished artworks. However, nowadays the visualization of these hidden drawings can provide a great deal of information about an artist's working process, by revealing how carefully a composition may have, or have not, been planned. What is more, they can provide evidence concerning the presence –or not– of more than one artistic hand, and also they may document changes made between the design stage and the final stage of the creation. All this extra information provides a whole new world waiting to be explored by the conservators, who are able to extract more details about the psychosynthesis or the mood of the painter, his methods and the way he proceeded during the formation of his creation. Additionally, the mapping of well-known paintings of popular artists, can dictate the working style of each artist, and this can be further used in order to prove the authenticity of newly discovered paintings, or in general, artworks whose authenticity could not have been proved with traditional means.

1.2. Drawing materials and Grounds

1.2.1. Drawing materials

Graphite is a crystalline form of carbon which is widely distributed naturally as a mineral in different parts of the world. Nowadays, the most important source is Sri Lanka; European sources have been Cumberland, Bavaria, and Bohemia, where deposits have been worked for centuries. Graphite can also be made artificially by a furnace process since about 1891. Graphite has long been used as a writing material and it gets its name appropriately from the Greek word “γράφειν” (= “to write”). It was early confused with lead, which was also

used for writing purposes, and hence the names “black lead” and “plumbago” are also used for it. Graphite has a greasy texture and is dull gray. It is one of the most stable and refractory materials and would be permanent in any technique. It has been used chiefly as a drawing material.

Carbon Black includes various pigments that are derived from the partial burning or carbonizing of natural gas, oil, wood, and other organic materials. Almost none of these products are pure carbon. Carbon makes a very stable pigment, that it is unaffected by light, air, or by hot concentrated acids and alkalis. It can only be destroyed if it is exposed to high temperatures (~700°C).

Silver Point has been the most common of the metal points used for drawing. In all of them the principle is the same. When the silver point is drawn over a properly coated ground (with very lean structure), fine particles of the metal are taken off and left in the line that has been described. It is a pale gray mark which in time corrodes slightly to a darker value and a warmer tone.

Ink is a liquid or viscous material used for writing, printing, lithographing, stamping, and staining. Inks are made from dyes and from pigment suspensions, like carbon black. Those used for printing and lithographing are made by grinding pigments in oils and varnishes. Ordinary writing inks are iron gall inks, in which the color and stain are formed by the combination of gallotannic acid (one of the two forms of tannic acid) from oak galls and green vitriol in the presence of air.

Lamp Black is nearly pure (over 99%), amorphous carbon which is collected in brick chambers from the condensed smoke of a luminous flame from burning mineral oil, tar, pitch, or resin. It is slightly bluish in color, and makes good neutral grays. Microscopically, it is very finely divided, uniform, and homogeneous; in mounting mediums, the particles appear to collect in chains and filaments. It does not wet well with water on account of the slight amount of unburned oil it contains.

Chalk is a natural deposit, a slaty, soft, earthy material and is very rich in carbon. It is widely used for drawing. As now prepared for the market, the various colors of drawing chalk are put up in small sticks or as pencils. Their use dates back to ancient times and they were as well very common during the Renaissance.

Charcoal Black is the residue from the dry distillation of woods and is made by heating the wood in closed chambers or kilns. When produced from smooth wood such as willow, bass, beech or maple it has the best quality. It may be used in stick form for sketching purposes and for the preparation of cartoons.

Vine Black, which is similar to charcoal, is prepared by carbonizing vine twigs or vine wood. Other similar vegetable blacks are made from peach stones, cocoanut shells, cork, etc.

Ivory Black was made by charring chips of ivory, its use was established in antiquity by the example of Apelles, but there is no evidence that it was continued in the Middle Ages. The standard black pigments of medieval times may be taken as lampblack and charcoal, each

from several sources, with lampblack from oil and charcoal from vine sprigs probably in the lead.

Crayon is a small stick for drawing, composed usually of pigment in an oil or wax. It is smooth and ordinarily used on paper. The use of crayons in Europe evidently began in Italy in the middle of the sixteenth century. Another type of crayon was made in the seventeenth century by dipping and cooking charcoal in linseed oil.

Sinopia (also known as sinoper, named after the now Turkish city Sinop) is a dark reddish-brown natural earth pigment, whose reddish color comes from hematite, a dehydrated form of iron oxide. It was widely used in Classical Antiquity and the Middle Ages for painting, and during the Renaissance it was often used on the rough initial layer of plaster for the underdrawing for a fresco. The word came to be used both for the pigment and for the preparatory drawing itself, which may be revealed when a fresco is stripped from its wall for transfer.

1.2.2. Grounds and carriers

The word "ground" when used about paintings –or works of art in general- is a little ambiguous. For example, is a picture is painted on a brick wall covered with plaster, either the brick or the plaster might be called the ground. By common consent, however, nowadays, the plaster in this case is called the "ground", and the brick wall the "carrier." Thus, in a panel painting, the wooden panel is called the carrier, and the layer of gesso, or plaster, or whatever there may be between the wood and the painting, is called the ground. (Grounds on canvas are still usually called "primings"). Sometimes there is no distinction, and others, the carrier itself is also the ground. The latter appears most commonly in writings, drawings or paintings on paper or parchment.

Canvas is, literally, a coarse cloth made from cotton, hemp or flax. This definition serves well enough to describe the traditional fabric used as a paint support in Europe, though hemp fiber is rarely found in such objects. The word 'canvas' has now a number of meanings. It may be used for artists' canvas or for a picture painted on canvas.

Palimpsest is a manuscript page, usually from parchment or paper, from which the original text has been scored and scratched to provide a good bond for the new, and the old surface ruthlessly covered and repainted. Sometimes the older members of these palimpsests have not been roughened, but simply plastered over, or even simply whitewashed, in preparation for the new decoration. Repainting of this sort has sometimes had the effect of preserving for us paintings or texts which might otherwise have been lost.

Lime is the standard medieval binding medium for wall painting. If a particle of pigment is surrounded by lime water, and the water dries away, the particle of pigment gets caught in the net of lime crystals. This binding effect may be accomplished by two methods. One is to mix lime water with the pigments; and the other is to mix the pigments with plain water only and apply them to fresh lime plaster. In this second case, the water with which the pigments are mixed mingles with the lime-saturated moisture of the fresh plaster, and the amount of lime mixed with the colors as a result is usually the minimum. There is no excess of lime to cloud or dull them, as there is apt to be when they are deliberately mixed with lime or lime

water before they are applied. Furthermore, they dry with the plaster, as a part of it, and not as a surface layer, more or less detached from the wall itself, as in the first system.

Nevertheless, a great deal of medieval painting was done on walls which had previously dried. The wall was damped down with lime water and a little lime or lime water was mixed with each color as it was applied. There is abundant evidence that this was the dominant method of European wall painting in the Middle Ages. Its chief rival, were oil painting, in England and Northern Europe and, after the beginning of the fourteenth century, in Southern Europe, the process known as buon fresco ("true fresco") painting.

True Fresco first appeared in the fourteenth century in Italy and it became a common practice to plaster walls in bits, and to paint on the fresh plaster with untempered colors, simply mixed with water, leaving the lime of the plastered wall to act as the binder for the pigments.

In true fresco, the artist draws his work full size on the rough plaster foundation, and covers only so much of it with fresh plaster as he hopes to be able to finish in a day. He undercuts the edge of each section as he finishes it, and interweaves the adjoining plaster neatly under the cut edge of previous days' work. True fresco may be recognized by the division of the painted surface by these joints between successive pieces of fresh plastering; but this is not binding, as many works called fresco will be found to have been executed by other means. For instance, joints of this sort appear in lime paintings which are not true fresco. They simply mean that parts of the painting were unsatisfactory, so that they were cut away, replastered, and painted over.

Secco Painting: To supplement the painting methods which depended on the binding action of lime, egg tempera was used on walls; but this method of painting involved hard work and was generally confined to developing an effect already partially established. Certain colors, especially blacks and blues, were dulled and dimmed by the whiteness of the crystallized lime binder, and they were usually applied with egg or size. Lime painting, whether on a dry wall or in fresco, did not lend itself readily to the deliberate execution of fine detail; and it was quite usual practice to depend on finishing with egg or size, until Renaissance times, when it became a popular "accomplishment", and finally an obsession, to complete a painting entirely on the wet plaster without retouching a secco.

1.3. Existing imaging techniques

As it has already been mentioned previously, the detection of underdrawings is a matter of great importance for restorers and thus, many techniques have been developed over the years, by several research teams. Each method has its advantages and drawbacks, depending on many parameters, that are about to be presented. As a result, the detection of the underdrawings of an artwork is usually realized in more than just one manner. What is more, different techniques provide the researchers with supplementary pieces of information. The most popular techniques used for imaging in cultural heritage are presented in the following pages.

1.3.1. Infrared Photography

First discovered in 1910s, infrared photography owes its existence to the American physicist Robert Williams Wood, who experimented with the infrared (IR) region of the electromagnetic spectrum. The irradiation of the specimen is done with lamps commonly used in photography, which produce light that appertains to the visible and IR spectrums. Part of the radiation is absorbed by the specimen, while the rest is reflected and then, it is being recorded on a camera film with spectral range up to 900nm. With the use of the proper filter, the visible part is cut-off of the camera lens, and hence, only the IR is collected. The use of this technique on paintings can provide additional information concerning the potential existence of cracks in the upper layers of the pigment. Hence it is considered as an important tool for paintings' preservation and restoration.

Figure 2: "The Good Samaritan".

During the irradiation of the sample, a number of optical phenomena can be observed, such as light absorption or reflection and, of course, scattering. At the IR region the percentage of light that is being absorbed or scattered is relatively lower than the percentage of the visible spectrum. Thus, IR radiation can penetrate and reach deeper into the painting. During the transmission through the volume of the painting a percentage of the IR radiation is again reflected and absorbed, but a sufficient amount reaches the depth where the underdrawings lay. The materials used for the underdrawings (like charcoal or graphite) have high absorption coefficients in IR, unlike the pigments that lay above. Infrared Photography is a non-invasive, non-contact technique, as the painting is not touched during the procedure. What is more, the photos can provide information about the exact location of the underdrawings relatively to the visible area of the painting, as the image resembles to a superposition of the different layers of the painting. Nevertheless, this superposition can potentially confuse the observer, because he cannot distinguish from which depth originates every piece of information. Also, the areas underneath darker pigments (like dark green, blue, black etc.) appear a lot darker, and thus the technique is efficient in colors like red, brown and white. Finally, the penetration of the IR radiation is related to the depth of the total paint layer. This is why it is not possible to acquire sufficient information from paintings with many layers of pigments with IR photography. The attenuation of the radiation in this case happens due to the scattering of the

Figure 3: IR Photography of a detail of the artwork. The lines and curves drawn by the apprentice are visible on every part of the body of the wounded Jew.

light during its transmission in the paint layers.

A beautiful example where the IR Photography was used is the painting “The Good Samaritan”, which has been attributed to a follower of the Dutch painter Jan van Scorel. The artwork was created in 1537. It is interesting to mention the fact that after the detection of the underdrawings, the researchers mentioned that they could distinguish between the sketches these that had been drawn by the apprentice and the ones made by Scorel himself. These where used by the follower as guidelines in order to create his work of art. Most importantly, though, the researchers brought to light certain features of this artist's working procedure. The underdrawn figure of the wounded man has a narrower waist, tapering limbs, and hands and feet half the size of their painted counterparts. In other words, the proportions of the underdrawn figure are at first glance more closely related to Scorel.

1.3.2. Infrared Reflectography

Infrared Reflectography (IRR) has been investigated since the 1960s, although the origins can be traced back to the 1930s, when IR photography was first proposed for the detection of underdrawings. The technique follows the same rules as IR Photography concerning the irradiation of the painting and the scattering, reflecting and absorbing phenomena that take place. In particular, the IR Reflectography, thanks to the properties of transparency of the pigments to the infrared radiation, allows the visualization of features underneath the surface of paintings, such as the underdrawing sketch, or subsequent repaintings. The main difference between the two techniques lies in the method of detection of the reflected light. In IRR, the collection of the reflected radiation occurs with a specific imaging system (that consists of optics and a camera) sensitive in the spectral region of approximately 2μm. The detection system converts IR radiation in visible and presents the result on a screen. The detection ability of the underdrawing, like in IR photography, is reduced while the depth of the paint layers is augmenting. What is more, the detection ability is inversely proportional to the absorbance coefficients of the paint layers. The advantage of IRR compared to IR Photography is that IRR has the means to provide information from other regions of the artwork, which are covered with blue or green pigments. It is important to

Figure 4: “Carrying of the Cross”.

Figure 5: left: Photograph of a selected area of the painting. right: IR Reflectogram of the same area presented on the left, where the underdrawing is visible.

underline the fact that the technological advancement of the IR detectors through the years has given the analogous enhancement at the results. Still though, the final image that is produced cannot separate the upper from the lower layers and thus it appears as a superposition of the sum of the paint layers and the underdrawings.

An interesting example of the IRR is Jan van Scorel's "*Carrying of the Cross"* (1530, oil on panel, 48.3x32.9 cm. Private collection, New York.). In Figure 5, a detail of the artwork is featuring the original and the IRR image respectively, where the hidden sketches are visible. The underdrawing on this work of art is loosely sketched in black chalk. It is not impossible that it was made by Scorel himself, but a shop assistant cannot be excluded. Another popular artwork where IRR was applied is the "Virgin of the rocks" by Leonardo Da Vinci. There are two versions of this painting, one at the Louvre Museum and the other at the National Gallery of London.

1.3.3. Multispectral Infrared Reflectography

Multispectral Infrared Reflectography, also known as Multispectral Imaging (MSI) is a commonly used technique in the domain of underdrawings detection. It got to the forefront of the branch of Cultural Heritage at the beginning of 1990. It is obvious from its name that the technique is based on the foundations of IR Reflectography. The difference of the two methods lies in the readjustment of the Multispectral IR Reflectography into a technique which acquires multiple images in different, narrow spectral bands of the IR spectrum. It was first applied for qualitative comparison of the different bands, in order to identify areas of different material composition, natural degradation, past conservation intervention, preparatory sketches, and quantitatively for improved precision in color measurement. Later, with increased number of bands and speed of acquisition, it was used to extract spectral reflectance information for pigment identification. The spectral images that are acquired in the different bands are stacked in a spectral cube where the x and y axes represent a point on the image and the z axis shows its reflectance over each spectral image. The final composition provides information that exceeds our knowledge due to IR Reflectography. The technique can be used for the analysis and authentication of pigments in paintings. MSI encounters the same limitation because of the light scattering and reflection as IRR, and this is why the technique cannot be used in works of art with thick or numerous paint layers. An example of the use of the MSI is a painting by Carlo Crivelli, "Saint Mary

Figure 6: "Saint Mary Magdalene".

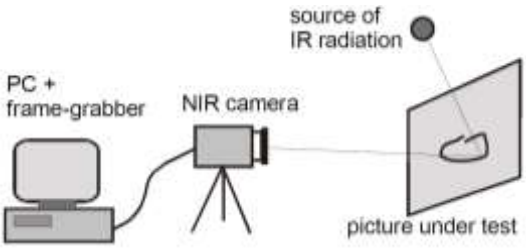

Figure 7: Typical configuration of an IRR system.

Magdalene" [Fig. 6] from the National Gallery of London (NG907.2).

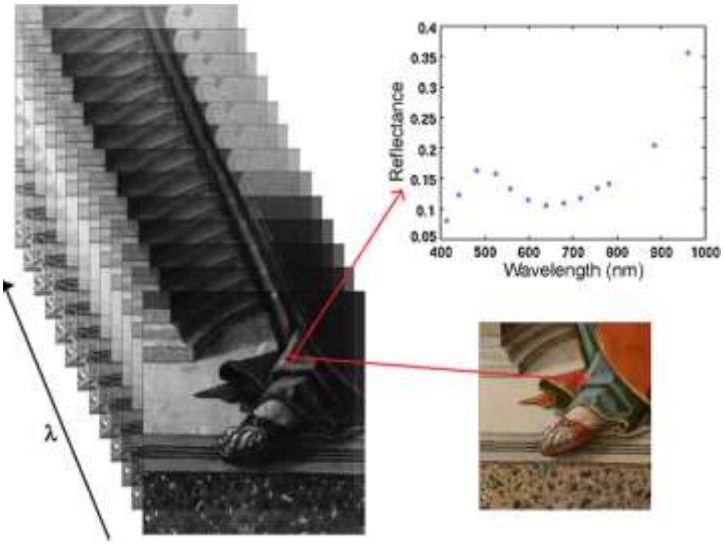

Figure 8: A schematic diagram illustrating a spectral cube obtained from multispectral imaging, the color image derived from the spectral cube and a spectrum for a point on the blue color which can be identified with the pigment "Azurite".

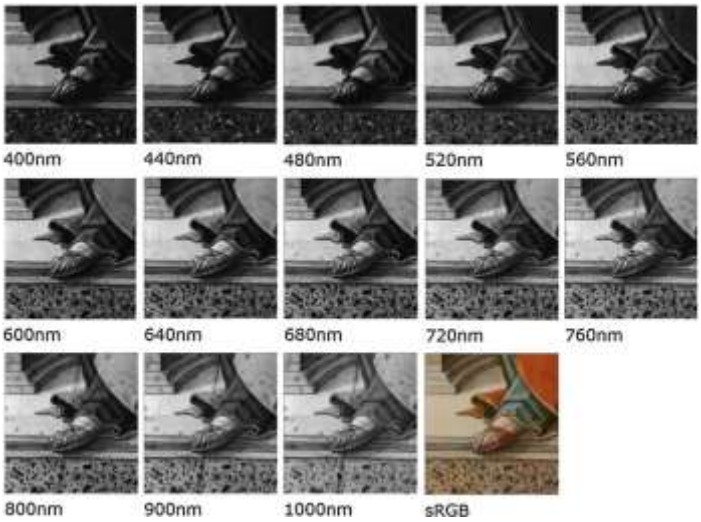

Figure 9: Detail of the painting on the left, acquired in different spectral bands.

1.3.4. X-Ray Fluorescence

In X-Ray Fluorescence (XRF) the sample is irradiated by an intense and focused X-Ray beam. The energy of the X-Rays is sufficient to expel electrons from the inner shells (close to the atomic nucleus) in an atom. Electrons from outer shells fall subsequently into the holes left by the expelled electrons and emit X-Rays in the process. As every atom has its own particular structure of its electron shells, the energy of the emitted X-Rays is characteristic for each element and can be used for its identification.

A characteristic example of the application of XRF is a painting created by Vincent Van Gogh in 1887, named "Patch of grass" (Kröller-Müller Museum, Otterlo, The Netherlands). The red frame in Fig. 10 indicates the field of view in Fig. 11, if the painting is rotated 90° counter-clockwise. The researchers that revealed the hidden painting reported the fact that it is

thought that one third of Van Gogh's known paintings seem to hide underneath their paint layers compositions of his early period of creation.

Figure 10: "Patch of Grass".

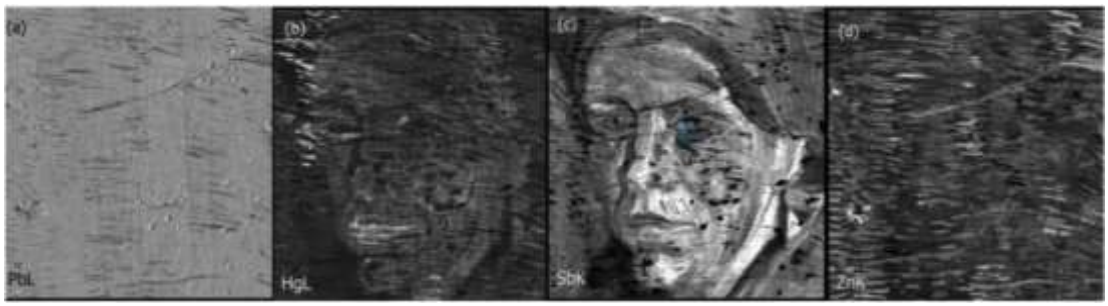

Figure 11: (a) Distribution of Pb L-edge measured with SR-based XRF (black corresponds to low intensity, while white, to high). (b) Hg L-edge indicates the distribution of vermillion. (c) Sb K-edge shows the distribution of Naples yellow, the paint sample location is indicated in the blue frame. (d) Zn K-edge indicates the distribution of zinc white, mostly corresponding with the surface painting, but there is some overlap with the concentration of SbK (nose, ear, neck).

1.3.5. Optical Coherence Tomography

Optical Coherence Tomography (OCT) is an optical interferometric technique, that is able to provide information about the varnish that exists over the paint layers on an oil painting, as well as about the existence of underdrawings behind the paint layers of a painting, via the creation of a 3-dimensional image of the layers of which the painting is consisted. Specifically, the sample is being irradiated with coherent radiation (usually in the NIR) with high pervasiveness. After, the scattered radiation from the specimen is detected. OCT has mostly been used in biological applications. Its appearance in cultural heritage emerged during the last years as if offers the possibility of a 3-dimensional mapping of the layering of

Figure 12: "The arrest of Christ".

the painting. In this way the underdrawing can be distinguished from the paint layers.

"The arrest of Christ" is a painting created around 1520 by an anonymous artist. It contains several layers of material, including an underdrawing executed in a dry medium, paint, as well as varnish. Fig. 13a shows a single cross-sectional image through the underdrawing feature which lies inside the red square of Figure 12, with three distinct layers visible. From top to bottom, these layers consist of varnish, paint, and underdrawing.

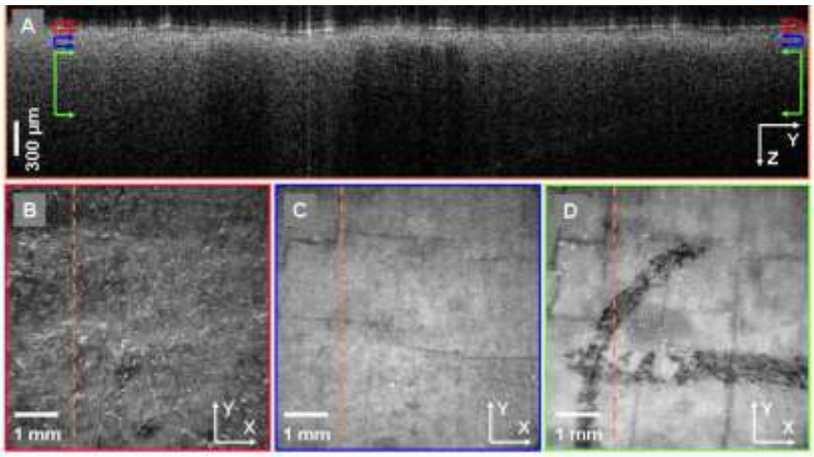

Figure 13: OCT images of the underdrawing feature in "Arrest of Christ." (A) Single cross sectional image taken through the underdrawing. Colored arrows indicate the locations of the varnish (red), paint (blue), and underdrawing (green) layers that were axially summed to form the summed voxel projection en face images in (B)-(D). (B) Summed voxel projection en face image of the varnish layer. (C) Summed voxel projection en face image of the paint layer. (D) Summed voxel projection en face image of the underdrawing layer. Orange dashed line indicates the location of the cross-sectional image in (A).

1.3.6. Terahertz Radiation

During the last decades, many research groups have been interested in studying samples in the domain of Terahertz Radiation. It is a nonlinear imaging technique, with wavelengths that lie at the far end of the infrared band, just before the start of the microwave band. The use of this kind of radiation provides greater penetration in comparison to the IR methods, and due to the fact that the energy of THz photons is lower, and thus more safe, the technique has already been used for many applications. One of the biggest advantages of THz Radiation is that due to the fact that it consists of submillimiter waves, it can penetrate through a wide variety of materials such as paper, wood, clothing, plastic and ceramics, which are usually opaque to both visible and infrared radiation.

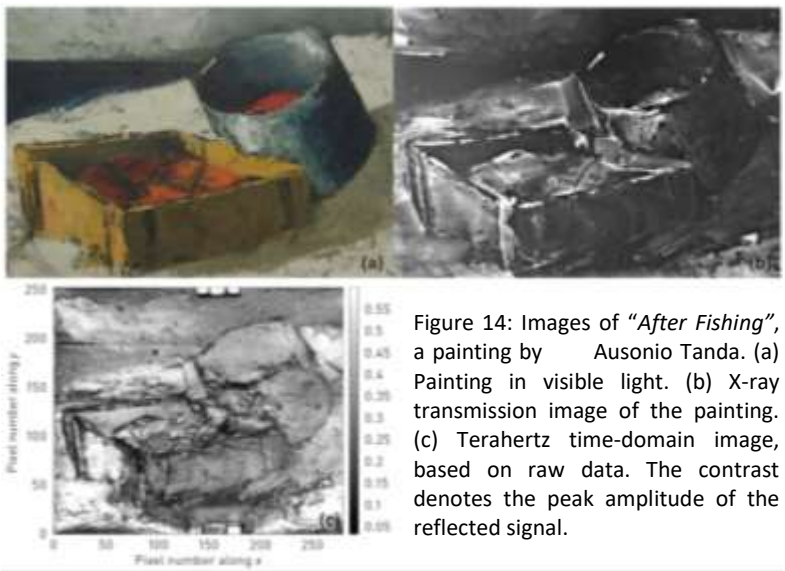

Figure 14: Images of "*After Fishing*", a painting by Ausonio Tanda. (a) Painting in visible light. (b) X-ray transmission image of the painting. (c) Terahertz time-domain image, based on raw data. The contrast denotes the peak amplitude of the reflected signal.

THz Radiation has already been used for the detection of text in papyruses and parchments that had endured severe external damages, for the calculation of the thickness of paint layers in paintings as well as for the detection of cracks on them. In comparison to X-rays and microwaves which can penetrate thick layers and are often used to reveal hidden underdrawings below the painting layers of an artwork, find dislocations, water damages and other defects, THz exhibit better depth and lateral spatial resolution. These transmission properties of the THz radiation in combination with the fact that information can simultaneously be obtained for the internal structure of an artwork, point out the potential of THz waves to become an essential tool for art analysis in the near future. Fig. 14 presents an example of the use of the technique on the painting "After Fishing", made during the 20th century by the artist Ausonio Tanda. The artwork consists of thick layers of paint, built up with a palette knife instead of a paintbrush.

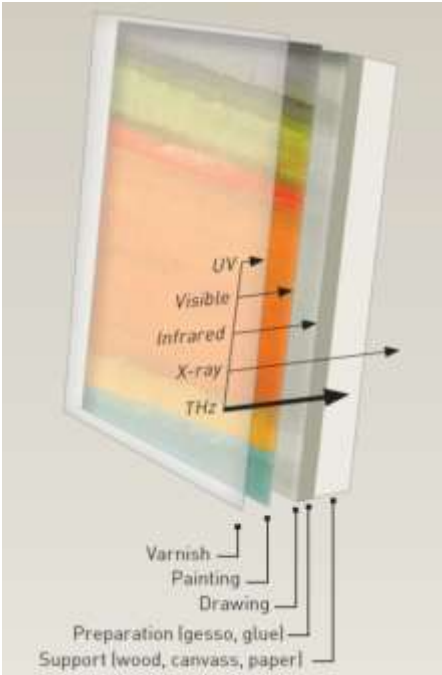

Figure 15: Cross-section of a typical painting, showing the penetration of different types of electromagnetic radiation. Terahertz rays travel farther into the layers than shorter frequencies of light. Although X-rays penetrate artifacts to greater depths, care must be taken with this ionizing radiation.

1.3.7. Preexisting Photoacoustic system

As it has already been mentioned, during the last years, with the cooperation of several I.E.S.L.-F.o.R.T.H. researchers and students of the UoC, a primitive imaging system based on the PA effect has been created. There are two possible geometries concerning the detection of the ultrasounds; a) detection from the rear side of the sample (transmission configuration) and b) detection from the front side of the sample (reflection configuration, also known as "epi-illumination"). The transmission system presented interesting and

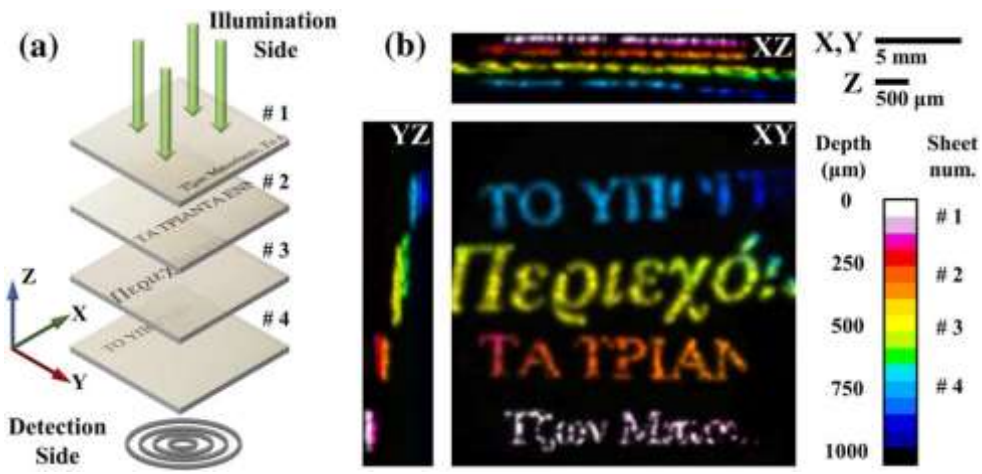

Figure 16: Depth colour-coded PA reconstruction of a four-layered document sample with nonoverlapping text (a) Schematics of sample's configuration. (b) Photoacoustic images in top (XY) and side (XZ, YZ) views. Imaging depth is measured starting from the page facing the illumination side.

promising results. Except for the imaging of underdrawings of paintings, the transmission set-up also had the capacity to detect and separately depict the produced PA signals which originated from layered sheets of paper [Fig. 16]. The epi-illumination set-up that has been developed, though, was comprised of spare components from other projects and thus it was in need of optimization.

1.4. Limitations of existing techniques

The aforementioned techniques present certain limitations. The fact that IR Photography, IRR, and MSI are based on the same principles denotes that these methods face the same constrains. Even though they are widely used for diagnostic purposes on cultural heritage, they are not efficient for a number of applications. To begin with, all the aforementioned techniques depend on the penetration of IR radiation, which is reduced as the paint layers - and everything else that might exist over the underdrawing, such as binders, varnish etc- increase, due to scattering phenomena. Even if a significant percentage of the initial light reaches the depth of interest though, the next obstacle that it has to overcome is to travel all the way to the corresponding photodetector, while facing again all the phenomena mentioned before. Thus, the absence of underdrawings in a certain area of the acquired image with the use of these techniques does not necessarily mean that there is none at the measured area of the artwork. This is the main reason why these techniques cannot be used for mural paintings, where the paint layers are, in general, thicker.

The optical limitations due to scattering and reflection of the radiation are present in OCT as well. What is more, OCT can only provide information for the underdrawings after the acquisition of successive measurements and their combination. Since each measurement is a perpendicular cross-section (as the one presented in Fig. 13A) of the stratigraphy of the artwork, in order to create the final composition a complicated post-processing is needed. The imaging of underdrawings is thus not the main aim of OCT, as it is a time-consuming and complex process.

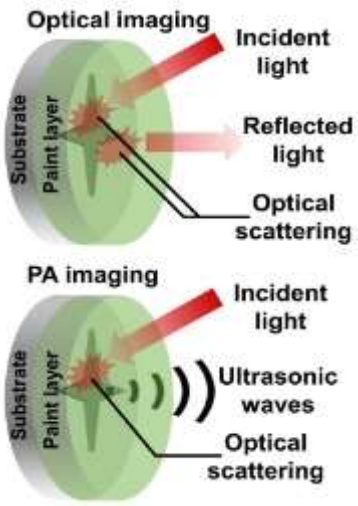

Figure 17: The advantage of PAI over the optical imaging technics

THz radiation is a promising technique that has a lot to offer in the field of cultural heritage. A significant challenge of the technique, according to Dr. Jackson, is the fact that there is a relative lack of published standards related to THz spectroscopy. Only a few THz spectroscopic databases, including one compiled by NICT and other Japanese institutions, exist online, but their entries range in number from a couple dozen to a couple thousand, which means that they are hardly enough to cover all the pigments, binders and residues that an archaeologist or art conservationist might encounter. Establishing standard spectra for materials in any wavelength regime is a challenge full of multi-instrument error analysis and grunt work.

An objective of the current dissertation is to convince the reader of the importance of the developed robust PAI system, since its applications could bring to light useful insight regarding the imaging of underdrawings of artworks with arbitrary geometries and also, it could be used for the recreation of the stratigraphy of complex samples in a non-destructive way.

2. Theory

2.1. General information

The PA effect is a phenomenon discovered in 1880 by A. G. Bell accidently, while he was working on the development of the "photophone", a device that allows transmission of speech on a beam of light. Initially the name of the phenomenon was "optoacoustic effect", but in time it was changed to "photoacoustic", in order not to be confused with the "acousto-optic effect", which refers to interactions of light with disturbances that are induced to an acousto-optic crystal because of sound waves. Bell and his partner, S. Tainter, observed that the PA effect is greatly dependent on the absorption of the radiation. What is more, they noticed that the power of the acoustic signal depends on the percentage of light that is being absorbed. Thus, they concluded that the source of the radiation determines the type of sound that is being produced. The PA effect was soon forgotten though, and it wasn't until after the emergence of lasers, approximately in 1960, when the phenomenon begun to be broadly used in different fields. Specifically, in 1963 R. M. White discussed about the production of high frequency sound waves in a solid medium as a result of the absorption of electromagnetic radiation. After that, it reappeared in 1967, when M. J. Brienza and A. J. DeMaria proved that pulsed Q-switched lasers can be used for the production of intense ultrasound waves during the heating of metal films that were placed on the surface of piezoelectric crystals. Through the irradiation with repetitive ns pulses, they managed to produce sound from solids at frequencies higher than 2 GHz. In 1977 R. J. Von Gutfeld and R. L. Melcher proposed for the first time that the PA effect could be used as an imaging method, based on White's results. They found that the strength of the acoustic signal could be increased by a large factor if the impedance of the material on either side of the absorbing layer was carefully controlled. They suggested that photoacoustic signals generated in this manner could be used in a system for imaging material defects. Wickramasinghe et al. converted a conventional acoustic microscope into a novel, photoacoustic one, used in transmission mode. The process they followed involved the subtraction of the input acoustic and its replacement by an optical objective lens. In this

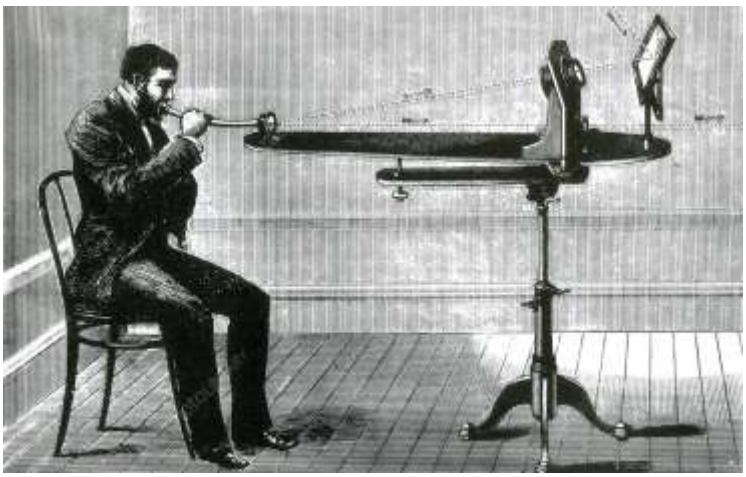

Figure 18: A.G. Bell conducting experiments with the photophone.

way, an optical input beam of a mode-locked Q-switched Nd:YAG laser was focused in a circle, with a diameter of 2 μm. During the experiments, the sample was being scanned mechanically while the detection of the produced acoustic waves was done with a transducer from the initial microscope. During the time of the realization of these experiments, the photoacoustic microscopes were being used to detect either the acoustic or the optical image, not a combination of both. With the use of a photoacoustic microscope adjusted at 50 kHz – 10 MHz, it was possible to produce images through the recording of the thermal waves which were created during the illumination of the sample at areas with different absorbing properties, due to the PA effect. Thus, in 1979 Rosencwaig proposed the idea of a microscope with a system of piezoelectric detection that could provide information about both the surface and the internal structure of the sample.

The PA effect is the production of acoustic waves after the absorption of light with time-variant intensity, in a transmission medium. The amplitude of the produced PA wave is proportional to the fluence of the laser (F) and the absorbance coefficient (μ). The amplitude is also determined by the isothermal compressibility (κ) and the thermal coefficient of volume expansion (β), which are thermodynamic constants. The produced waveform depends on the spatiotemporal characteristics as well as on the geometry (e.g. size, shape) of the absorber. The size of the absorber is inversely proportional to the frequency of the PA wave.

2.2. Ultrasound propagation

2.2.1. Acoustic waves

An acoustic wave is a type of pressure propagation by means of adiabatic compression and decompression. An acoustic wave travels with an acoustic velocity, which is characteristic of the medium. Acoustic waves are longitudinal and can be described using the following generic properties:

-amplitude (s_0): the maximum displacement from the equilibrium

-amplitude of pressure wave (p_0): the maximum pressure in comparison to the value at the

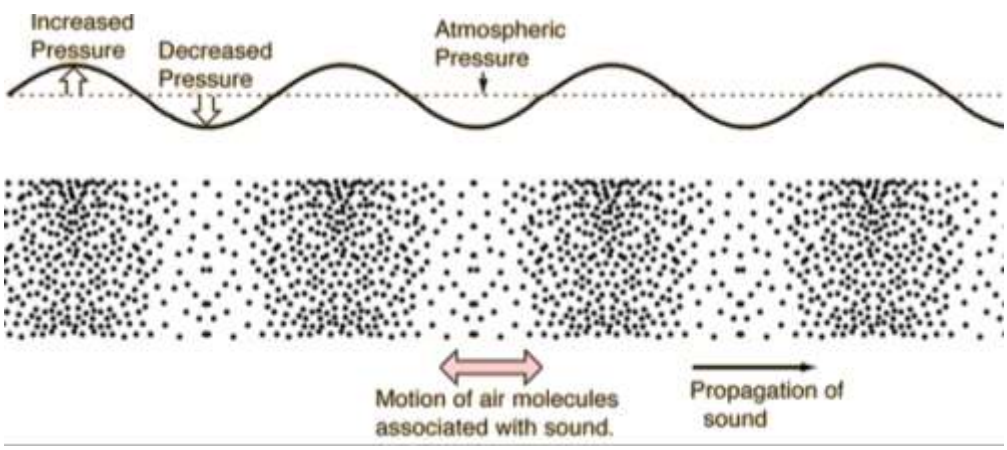

Figure 19: Propagating acoustic wave. In the areas were the density of molecules is high, the pressure is increased, whereas in the areas where the density of molecules is low, the pressure decreases.

equilibrium

-speed of sound (c): the propagation rate of energy in the transmission medium

-frequency (f): the number of cycles completed per second

-intensity (I): the emission or absorption rate of acoustic energy per second

Each medium is characterized by its specific acoustic impedance (Z), given by the following equation: $Z = \rho c$ (1), where ρ: the density of the medium and c: the speed of sound in the medium.

Ultrasounds are the acoustic waves with frequencies higher than the upper audible limit of the human hearing. Their frequencies vary from 20 kHz up to several GHz.

2.2.2. Reflection and transmission of acoustic waves

When an incident acoustic wave that travels in a medium with specific acoustic impedance Z_1 meets a second medium, with specific acoustic impedance Z_2, part of the wave is reflected back to the first medium and the rest refracted into the second medium. Snell's law, which is known for electromagnetic wave propagation, applies in acoustics as well: $\frac{\sin\theta_i}{\sin\theta_r} = \frac{c_1}{c_2}$ (2).

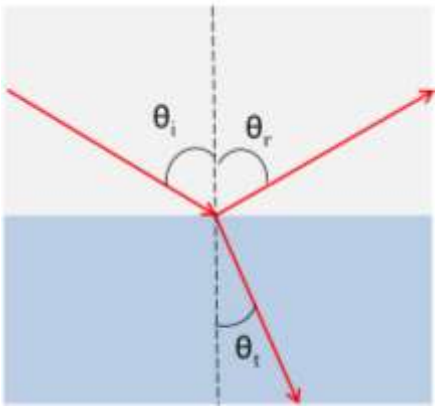

Figure 20: Reflection and refraction of an acoustic wave. θ_i: angle of incident acoustic wave, θ_r: angle of reflected acoustic wave, θ_t: angle of refracted acoustic wave (where t stands for transmission, as this part of the wave manages to pass from the first medium to the second).

When $\theta_t = 90°$, then $\theta_i = \theta_c$ (crucial angle) and $\sin\theta_c = \frac{c_1}{c_2}$. What is more, for $\theta_i > \theta_c$ and $c_2 > c_1$ the wave is not transmitted into the second medium. The percentage of the s_0 that is being reflected or transmitted is given by the following equations:

Transmittance coefficient:

$$T = \frac{p_t}{p_i} = \frac{2Z_2 \cos\theta_i}{2Z_2 \cos\theta_i + Z_1 \cos\theta_t} \quad (3)$$

Reflectance coefficient:

$$R = \frac{p_r}{p_i} = \frac{Z_2 \cos\theta_i - Z_1 \cos\theta_t}{2Z_2 \cos\theta_i + Z_1 \cos\theta_t} \quad (4).$$

Supposing vertical incidence, implicates that $\theta_i = \theta_t = 0°$ and the equations that were mentioned above can be simplified to: $T = \frac{2Z_2}{Z_2 + Z_1}$ (5) and $R = \frac{Z_2 - Z_1}{Z_2 + Z_1}$ (6).

What is more, for every possible pair of angles θ_i and θ_t, it can be shown that $T = 1 + R$ (7).

The percentage of the reflected or transmitted energy is given by Eq. 8 and 9:

$$R.E. = R^2 = \left(\frac{Z_2 - Z_1}{Z_2 + Z_1}\right)^2 \quad (8) \qquad T.E. = 1 - R^2 = 1 - \left(\frac{Z_2 - Z_1}{Z_2 + Z_1}\right)^2 \quad (9).$$

When $Z_2 - Z_1 \approx 1$ (i.e. $Z_1 \rightarrow 0$), it is evident from Eq. 8 and 9 that only an insignificant amount of energy manages to pass through the interface.

Fig. 21 presents an energy loss example of an acoustic wave due to the propagation through different media. In each step, the arrow is proportional to the energy of the acoustic wave.

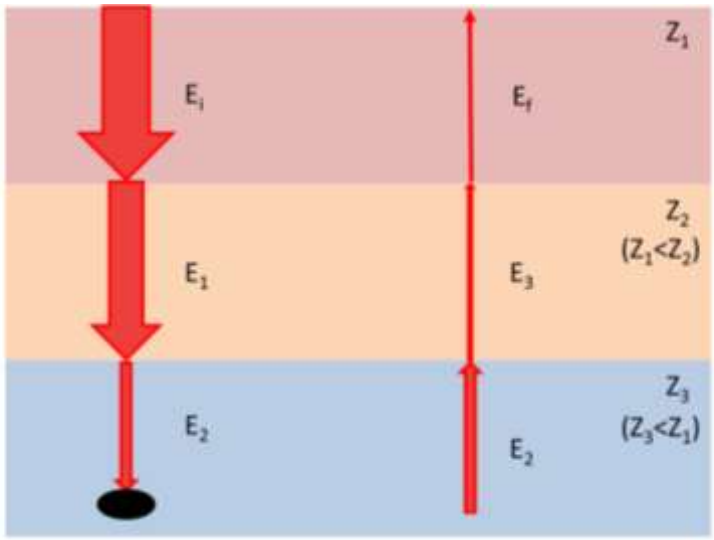

Figure 21: Energy loss example (assuming $Z_3<Z_1<Z_2$): An acoustic wave passes from medium 1, to mediums 2 and 3, it is then absorbed and re-emitted and then follows the opposite path - from medium 3 to mediums 2 and 1 -. In this example it is assumed that there is no energy loss due to absorbance into any medium, and that the absorber reflects 100% of the absorbed energy.

2.3. Derivation of the general photoacoustic equation

The PA effect is described by a partial differential equation known as "general photoacoustic equation", and it is derived from two equations.

The first one, is the thermal expansion equation $\nabla \cdot \vec{\xi}(\vec{r},t) = -\kappa \cdot p(\vec{r},t) - \beta \cdot T(\vec{r},t)$ (10), where $\vec{\xi}$ represents the medium displacement from the equilibrium state, κ is the isothermal compressibility, β is the thermal coefficient of volume expansion, p is the pressure and T, the temperature.

Isothermal compressibility is defined as: $\kappa = -\frac{1}{V}\left(\frac{\partial V}{\partial P}\right)_T$ (11) and expresses the fractional change of volume while changing the pressure at a constant temperature. Thermal coefficient of volume expansion is defined as:

$\beta = \frac{1}{V}\left(\frac{\partial V}{\partial T}\right)_P$ (12). It shows the way that a fraction of volume changes while temperature alters, at a constant pressure.

In order to extract the second equation we consider a cubic parcel of a medium, with mass m, equal to $m = \rho \cdot dA \cdot dz$ (13), where dA is the infinitesimal surface area, dz the height and ρ its density. By replacing Eq. 13 to Newton's 2nd law we get:

$F = \rho \cdot dA \cdot dz \cdot a$ (14).

It is also known that $F = p \cdot A$ (15). Thus, by combining the two equations we get:

$$-dp \cdot dA = \rho \cdot dA \cdot dz \cdot a \Rightarrow -dp = \rho \cdot dz \cdot a \Rightarrow \rho \cdot a = -\frac{dp}{dz} \quad (16).$$

In a more general form, Eq. 16 can be written as:

$$\rho \cdot \vec{a} = -\nabla p(\vec{r},t) \Rightarrow \rho \frac{\partial^2}{\partial t^2}\vec{\xi}(\vec{r},t) = -\nabla p(\vec{r},t) \quad (17).$$

Taking the divergence of (17):

$$\rho \frac{\partial^2}{\partial t^2}[\nabla \cdot \vec{\xi}(\vec{r},t)] = -\nabla^2 p(\vec{r},t) \quad (18).$$

Eq. 18 is called "inviscid force equation".

$$(10),(18) \Rightarrow \rho \frac{\partial^2}{\partial t^2}[-\kappa p(\vec{r},t) + \beta T(\vec{r},t)] = -\nabla^2 p(\vec{r},t) \quad (19).$$

If we arrange the terms more conveniently, we obtain:

$$\left(\nabla^2 - \rho\kappa \frac{\partial^2}{\partial t^2}\right) p(\vec{r},t) = -\beta\rho \frac{\partial^2 \mathrm{T}(\vec{r},t)}{\partial t^2} \quad (20).$$

From the Newton-Laplace equation we can derive the speed of sound: $u_s = \sqrt{\frac{K}{\rho}}$ (21), where K is the bulk modulus measuring the resistance of the medium to uniform compression. K is equal to the inverse compressibility (κ). Thus, the speed of sound can be expressed as $u_s = \sqrt{\frac{1}{\rho\kappa}}$ (22).

The final form of the photoacoustic equation is a result of the combination of Eq. 20 and 22 and it is shown below:

$$\left(\nabla^2 - \frac{1}{u_s^2}\frac{\partial^2}{\partial t^2}\right)p(\vec{r},t) = -\frac{\beta}{\kappa u_s^2}\frac{\partial^2 T(\vec{r},t)}{\partial t^2} \quad (23).$$

The left side of the equation describes the pressure wave propagation. The right side is the source term. We can easily conclude from the equation that time-invariant heating does not produce a pressure wave, only time-variant heating does.

2.4. Photoacoustic equation under thermal confinement

Under thermal confinement conditions, at which heat conduction is negligible during the laser pulse, we can derive from the fundamental equation $Q = mC_V \mathrm{T}$ (24) (where Q: thermal energy, m: mass, C_V: specific heat capacity under constant volume and T: absolute temperature) that:

$$\frac{dQ}{dt} = mC_V\frac{dT}{dt} = \rho V C_V\frac{dT}{dt} \quad (25).$$

We define the heating function H as the thermal energy converted per unit volume per unit time (S.I. units: $\frac{J}{m^3 s}$). The heating function combined with Eq. 25 results to:

$$H = \rho C_V\frac{dT}{dt} \quad (26).$$

It is also known from thermodynamics that:

$\frac{C_P}{C_V} = \frac{\kappa}{\beta_S}$ (27), where C_P and C_V are the specific heat capacities under constant pressure and volume, while β_S stands for the isoentropic compressibility, which is defined as

$$\beta_S = -\frac{1}{V}\left(\frac{\partial V}{\partial P}\right)_S \quad (28).$$

On the other hand, the equation of state (which gives us information about the relation of the thermodynamic variables) denotes that:

$$u_s^2 = \left(\frac{\partial P}{\partial \rho}\right)_S \quad (29).$$

By combining Eq. 28 and 29 we get:

$$\beta_S = -\frac{1}{V}\left(\frac{\partial V}{\partial P}\right)_S\frac{\partial \rho}{\partial \rho} = -\frac{1}{V}\left(\frac{\partial \rho}{\partial P}\right)_S\frac{\partial V}{\partial \rho} = -\frac{1}{Vu_s^2}\frac{\partial V}{\partial \rho} = -\frac{1}{Vu_s^2}\frac{\partial(m/\rho)}{\partial \rho} = \frac{1}{\rho u_s^2} \quad (30).$$

Eq. 27 and 30 will finally result in:

$$\kappa = \frac{C_P}{\rho u_s^2 C_V} \quad (31).$$

By substituting Eq. 24 and 31 to 23, the source term (right part) becomes:

$$-\frac{\beta}{\kappa u_s^2}\frac{\partial^2 T(\vec{r},t)}{\partial t^2} = -\frac{\beta}{C_P}\frac{\partial H(\vec{r},t)}{\partial t} \quad (32).$$

Thus, we conclude:

$$\left(\nabla^2 - \frac{1}{u_s^2}\frac{\partial^2}{\partial t^2}\right)p(\vec{r},t) = -\frac{\beta}{C_P}\frac{\partial H(\vec{r},t)}{\partial t} \quad (33).$$

From the form of this equation we can derive a result of significant importance; it is evident that for the production of a propagating pressure wave, a time-varying source of irradiation is needed. Otherwise, the right hand side of the Eq. 33 would be equal to zero, and thus, the photoacoustic effect wouldn't take place.

The quantity $H(\vec{r},t)$ can be further decomposed as the product of the respective spatial and temporal parts (separation of variables) in the following form:

$H(\vec{r},t) = H_S(\vec{r})H_T(t)$ (34), where $H_S(\vec{r})$ represents the local deposited energy density in J/m^3 and $H_T(t)$ is the temporal excitation profile.

Using Eq. 34, Eq. 33 can be written as:

$$\left(\nabla^2 - \frac{1}{u_s^2}\frac{\partial^2}{\partial t^2}\right)p(\vec{r},t) = -\frac{\beta H_S(\vec{r})}{C_P}\frac{\partial H_T(t)}{\partial t} \quad (35)$$

Eq. 35 compromises the photoacoustic equation under thermal confinement conditions.

Since each laser pulse can be ideally considered as a delta function, Eq. 35 is written as:

$$\left(\nabla^2 - \frac{1}{u_s^2}\frac{\partial^2}{\partial t^2}\right)p(\vec{r},t) = -\frac{\beta H_S(\vec{r})}{C_P}\frac{\partial \delta(t)}{\partial t} \quad (36).$$

This is the final form of the photoacoustic equation.

2.5. Requirements of effective heat production

From Eq. 10 we can conclude that if the laser pulse width is much shorter than both the thermal and stress relaxation time (no heat or stress escapes), the fractional volume expansion will be negligible; therefore the left part of Eq. 10 can be set equal to zero. Immediately after the laser pulse, assuming homogeneous illumination, the local pressure rise (p_0) can be derived as: $p_0 = \frac{\beta T}{\kappa}$ (37).

Using Eq. 24, then Eq. 37 can be further re-written in a temperature-independent form: $\Delta Q = mC_V \Delta \mathrm{T} \Rightarrow \frac{\Delta Q}{V} = \rho C_V \Delta T \Rightarrow \Delta T = \frac{\Delta Q}{\rho C_V V}$ (38)

The ratio Q/V reflects the thermal energy converted per unit volume and can be expressed as a function of the specific optical absorption A, which determines the amount of absorbed laser light per volume unit (S.I. units: J/m^3). If we express the previous sentence mathematically, we get: $\frac{\Delta Q}{V} = \eta_{th} A$ (39). η_{th} corresponds to the percentage of the absorbed optical energy that is converted into heat.

Thus, we extract from Eq. 38 that:

$\Delta T = \frac{\eta_{th} A}{\rho C_V}$ (40).

By combining Eq. 37 and 40:

$p_0 = \frac{\beta}{\kappa \rho C_V} \eta_{th} A$ (41).

Using Eq. 31 and 41, the initial photoacoustic pressure can be expressed as:

$p_0 = \frac{\beta u_s^2}{C_P} \eta_{th} A$ (42).

In order to simplify the calculations, we define $\Gamma \equiv \frac{\beta u_s^2}{C_P}$ (43) as the dimensionless Gruneisen parameter Γ and thus, Eq. 42 becomes: $p_0 = \Gamma \eta_{th} A$ (44).

If we consider stress confinement, the initially generated photoacoustic pressure will be proportional to $H_S(\vec{r})$ function, with proportionality constant the Grueneisen parameter Γ, which we previously defined. Thus, it is obvious from Eq. 42 and 43 that:
$H_S(\vec{r}) = \eta_{th} A$ (45).
By substituting the specific optical absorption A for the product $F\mu_\alpha$, where F is the optical fluence (J/cm^2) and μ_α corresponds to the optical absorption coefficient (cm^{-1}) for the employed wavelength, Eq. 44 can be rewritten as: $p_0 = \Gamma \eta_{th} \mu_a F$ (46).

By assuming uniform absorption properties of the object, $H_S(\vec{r})$ can be finally written as: $H_S(\vec{r}) = \eta_{th} \mu_a F(\vec{r})$ (47).

2.6. Spotsize and fluence calculation

The energy of the beam can be measured using a joulemeter. For the measurement, a diverging lens and the measuring instrument are placed right after the converging lens of the apparatus. The laser beam has an elliptical shape, and the axes were measured and found equal to $\mathrm{a} = 1.2\ \mathrm{mm}$ and $\mathrm{b} = 0.6\ \mathrm{mm}$. Using equation $s = \pi ab$ (48) – where s: the area of the ellipse – the spotsize of the laser beam is calculated and is equal to 2.3 mm^2. Hence, using equation $F = \frac{E}{s}$ (49) the fluence of the beam can be calculated.

The energy of the preexisting system was ranging between $\mathrm{E} = (1.73, 2.5)\mathrm{mJ} \pm 20\ \mu\mathrm{J}$, while the calculation of the new system showed that the energy values lied between $\mathrm{E} = (0.116, 0.345)\mathrm{mJ} \pm 20\mu\mathrm{J}$.

Thus the measurements of the preexisting system were realized with a fluence ranging between $(75.22, 108.70)\ \mathrm{mJ/cm^2} \pm 0.01\ \mathrm{mJ/cm^2}$, while the enhanced system's range was $(5.04, 15.00)\ \mathrm{mJ/cm^2} \pm 0.01\ \mathrm{mJ/cm^2}$.

2.7. Spatial resolution

The property that sets the spatial resolution is the impulse response of the imaging system or, more accurately, the characteristics of the image obtained when scanning an isolated point target. The obtained image in this case depicts a map of the combined effect of the physical processes involved and the reconstruction procedure. This map is known as the point spread function (PSF). The profile of the PSF along any direction depicts the "smearing" of the information along that direction due to the overall reconstruction process.

In the context of PAI, it is important to characterize the resolution along the beam direction, defined herein as the "axial resolution" and the resolution perpendicular to the beam, defined as the "lateral resolution".
Since the optical beam – even in the absence of scattering – is much wider than the acoustic focus, the lateral resolution of the system is given by $R_L = 0.71\frac{\lambda_A}{NA_A} = 0.71\frac{\upsilon_A}{NA_A f_A}$ (50), where NA_A is the numerical aperture of the ultrasonic transducer, υ_A is the speed of sound in the medium, and λ_A, f_A are the central wavelength and frequency of the PA signal, respectively. The constant 0.71 reflects the full width at half maximum (FWHM) of the acoustic focal spot in acoustic amplitude. In the system presented at this work, the bandwidth of the produced signal is wider than the transducer's. Thus, the calculation of the lateral resolution is defined by the central frequency of the transducer, which is $f_c = 10.6MHz$. Its diameter (d) is equal to 6.35mm and the focal length (f) is 1.23cm. The numerical aperture of the transducer is: $NA_A = \sin\theta$ (51). Since the angle θ is way smaller than 10°, the approximation $\sin\theta \approx \theta$ can be used and the numerical aperture can be computed using the following equation: $NA_A \approx \theta = \frac{d/2}{f} = 0.258$.

What is more, the speed of sound in water (at 25°C) is equal to 1498m/s. Hence, the diffraction limited value of the lateral resolution of our system is $R_L = 388.9\mu m$.
The computation of the axial resolution is done with the following equation: $R_A = 0.88\frac{\upsilon_A}{\Delta f_A}$ (52). This calculation is done based on the assumption that the PA response to a point target follows a Gaussian frequency profile. Δf_A is the bandwidth of the PA signal, which can be approximated as the detection bandwidth of the ultrasonic transducer and is often proportional to its central frequency f_A.

It is also known that the high frequency components of acoustic waves are attenuated faster in comparison to the low frequency components, and thus, the PA signal bandwidth decreases with imaging depth, resulting in worse axial resolution at greater depths.

For the transducer used in the current experimental apparatus $\Delta f_A = 1.1 \cdot 10^7$ Hz, and thus, the axial resolution of the system is: $R_A \approx 119.8\mu m$.

2.8. The Nyquist-Shannon Theorem

One of the most important rules of sampling is called "The Nyquist-Shannon Theorem". This theorem states that the highest spatial frequency of the specimen which can be represented accurately while preserving spatial resolution in the resulting digital image is one half of the sampling rate. The Nyquist rate specifies the minimum sampling rate that fully describes a given signal; in other words, a sampling rate that enables the signal's accurate reconstruction from the samples. In reality, the sampling rate required to reconstruct the original signal must be somewhat higher than the Nyquist rate, because of quantization errors introduced by the sampling process. As a result, if the sampling occurs at an interval beneath the number required by the Nyquist criterion, details with high spatial frequency will not be accurately represented in the final digital image.

2.9. Absorbance

2.9.1. Absorption spectra

Considering the fact that the transmission (T) for thick layers is zero, as the photons are not able to reach the rear side of the sample, it can be written that $R + A = 1$ (53), where R stands for reflectivity and A represents the absorbance. Thus, if the pigment used in the samples has a low value of reflectivity, it is more probable that a number of photons will achieve to reach the depth of the underdrawing, as they are absorbed not only at the interface of the sample and the environment, but also inside the volume of the pigment. The pigments that were used for the preparation of the samples have a reflectivity between 58% and 93% at 1064nm.Below are given the graphs [Fig. 22-25] of the reflectance spectrums of the pigments used in the samples that were measured with both versions of the system.

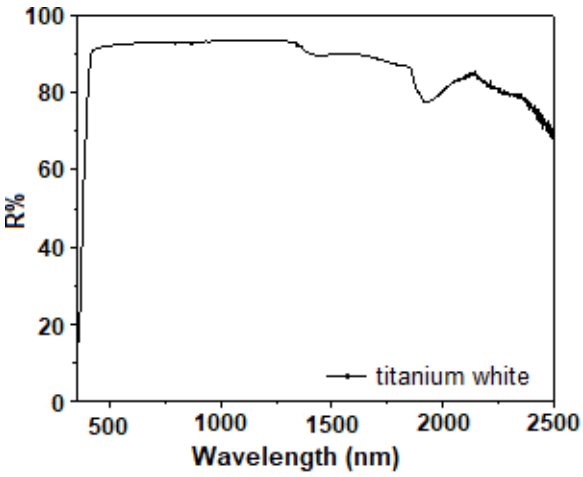

Figure 22: Reflectance spectrum of titanium white.

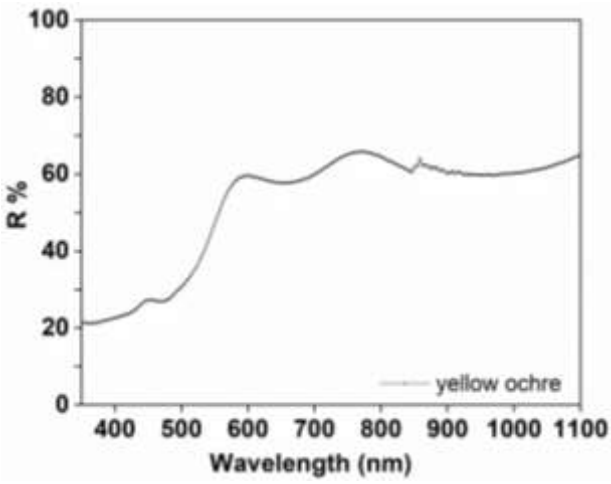

Figure 23: Reflectance spectrum of yellow ochre.

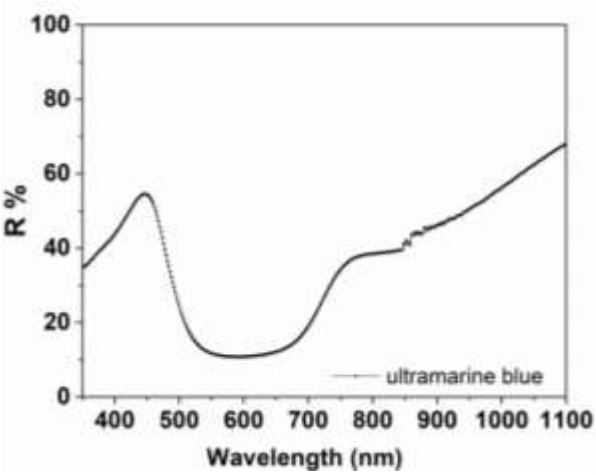

Figure 24: Reflectance spectrum of ultramarine blue.

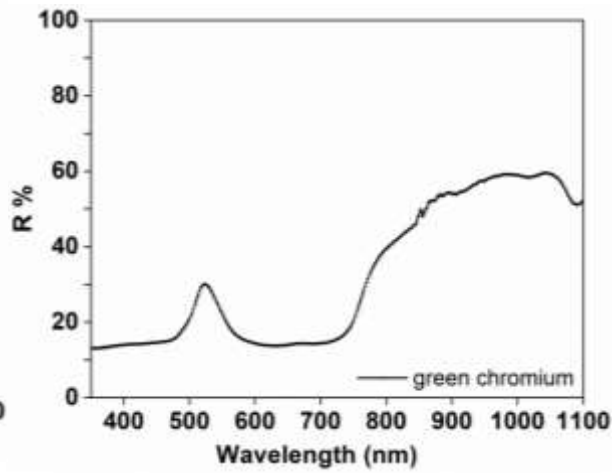

Figure 25: Reflectance spectrum of chromium green.

2.9.2. The Beer-Lambert Law

Generally, light absorbtion in a medium follows the Beer-Lambert law, meaning that the intensity of the light (I) at depth z, is comput $I(z) = I_0 e^{-\mu z}$ (54), where I_0: the initial value of the intensity (at z=0) and μ: the absorbance coefficient of the medium. The contrast of an image is proportional to the light that manages to reach the absorber.

3. Experimental setup

3.1. Developed system

The experimental apparatus [Fig.26] employs a Q-switched Nd:YAG laser source emitting infrared radiation at 1064 nm, with pulse duration equal to 10 ns. The selected Repetition Rate [RR] of the laser is 10 Hz. Before the irradiation of the sample, the beam is split by a beam-splitter. A percentage is led to a photodiode in order to acquire trigger and to synchronize the movement of the stages with the irradiation of each pulse. The rest passes through an attenuator. The energy is thus reduced to a level that is not destructive for the pigment of the sample. What is more, prior to the irradiation the beam is focused by a

converging lens (f=50cm). The sample is placed at the bottom of a rectangular tank made of aluminum, which is filled with distilled water. Water acts as the coupling medium, in order to ensure efficient transmission of the ultrasound signals that are induced by the laser. The tank is attached to a motorized XY micrometric stage (Danaher Precision 2198505 1.0A), which can scan a rectangular area up to 224 cm^2. The precession of the stage's step is approximately 1μm. For the detection of the generated photoacoustic waves, a single

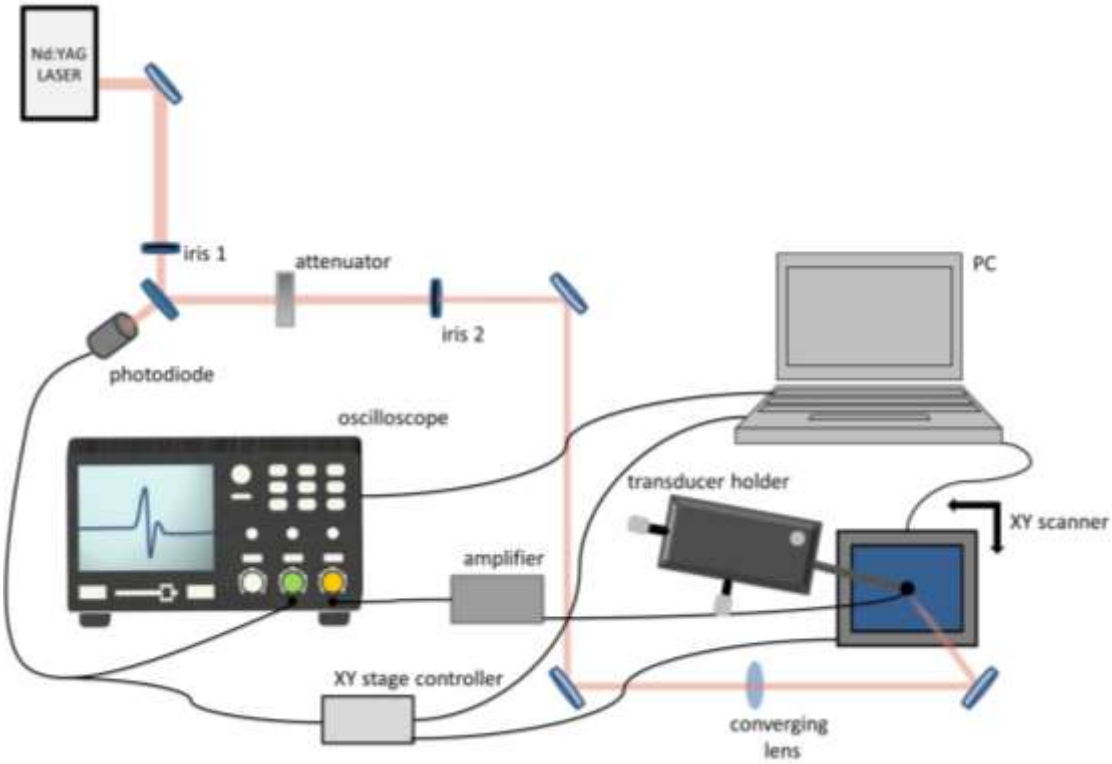

Figure 26: Visual representation of the experimental setup (M_i: mirrors, I_i: irises).

element spherically focused broadband ultrasonic transducer (OLYMPUS, Waltham, MA; central frequency: 10MHz, focal distance: 1.23cm) is immersed in the distilled water. The acquired time-domain signal is enhanced using a low noise RF amplifier (gain: 63 dB) and is then transmitted to an oscilloscope (Agilent Technologies) and recorded by a computer, using custom-made scripts. In order to improve the Signal to Noise Ratio (SNR), for each measurement sequential photoacoustic waveforms were averaged over 2 to 8 incident laser pulses, depending on the stability of the acquired signal.

3.2. Technical comparison between the two versions of the system

In this section, the two versions of the PAI system are compared in respect to the instrumentation, and their general efficiency. As it has been mentioned before, the preexisting PAI system was composed of spare components from different bio–imaging apparatuses. Thus, after the acquisition of a sufficient amount of data, the technical enhancements that could take place were revealed. The most apparent observation was the fact that the water–immersion transducer used in the preexisting system was not the ideal for this project. This transducer has its central frequency at 73MHz [Fig. 27], while the central frequency of the ultrasound that is produced by the graphite after the illumination with the laser is approximately at 6MHz [Fig. 28]. The cutoff frequencies of the

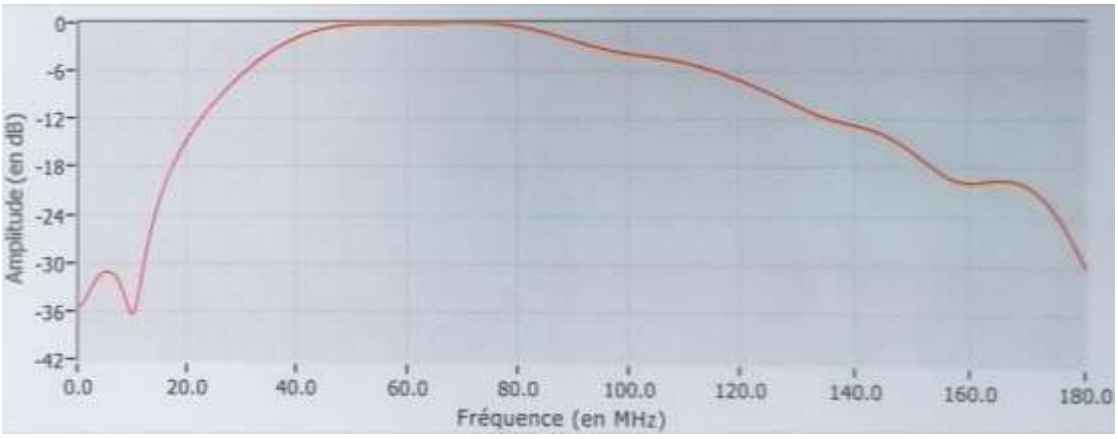

Figure 27: The bandwidth of the ultrasonic transducer used in the preexisting system. The horizontal axis represents the frequencies in MHz and the vertical the amplitude of the produced ultrasound, measured in dB.

aforementioned transducer are $f_{min} = 30.7\text{MHz}$ and $f_{max} = 115.3\text{MHz}$, as seen in Fig. 27, and they correspond to a spectral amplitude equal to half its peak value (i.e. to -6dB). By convention, it is considered that the transducer is more sensitive to the frequencies that lie between this range (and specifically, to these that are located near the center). Frequencies out of that region are able to be detected by the transducer, but their peak–to–peak value is lower. Thus, the efficiency of the acquired measurements is affected, since the frequencies are approximately one order of magnitude lower. As a result, the image does not have the optimum contrast.

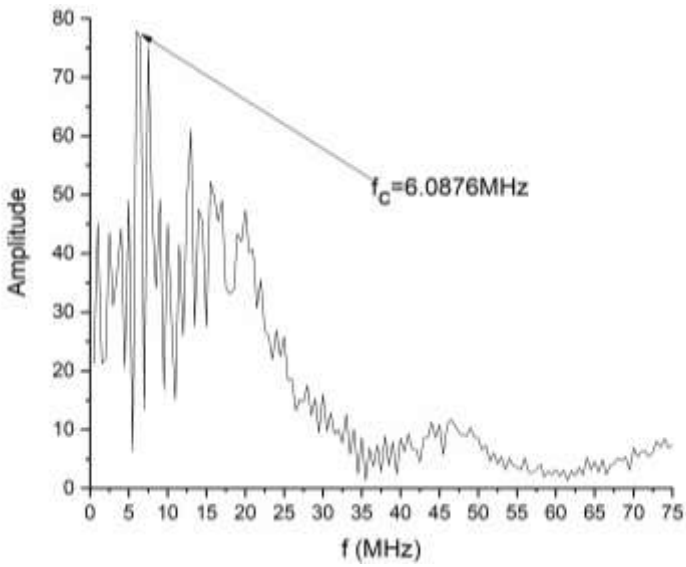

Figure 28: FFT of a typical PA signal acquired due to graphite illumination.
The central frequency is f_c=6.0876MHz.

The water–immersion transducer selected for the optimization of the system has its central frequency at 10.6MHz, while the cutoff frequencies are $f_{min} = 5.10\text{MHz}$ and $f_{max} = 16.10\text{MHz}$ [Fig. 29]. Thus, the developed system can detect much feebler signals and also, the acquired raw images have greater contrast compared to the previous ones.

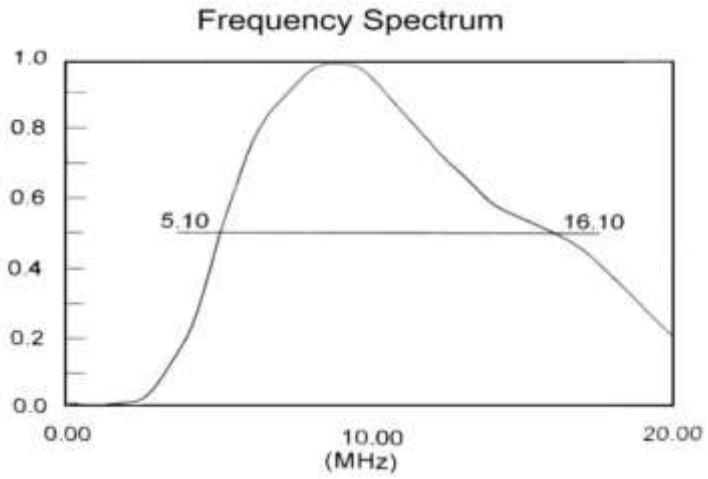

Figure 29: The bandwidth of the ultrasonic transducer used in the enhanced system. The horizontal axis represents the frequencies in MHz while the vertical axis represents the normalized amplitude of the produced ultrasound.

Another modification that took place for the enhancement of the preexisting system was the replacement of the micrometric stages which were being used, with others that are able to scan a wider surface; namely, the maximum scan area altered from 56.25cm^2 to 224cm^2. Furthermore, the replacement of the stages led to the development of new scripts. These new custom–made scripts altered the scanning method of the preexisting system, and at the same time, they significantly reduced the acquisition time. More specifically, the scanning of the samples was converted from point–by–point acquisition to continuous scanning. The resulting difference in the acquisition time provided the possibility to enhance the resolution of the developed system. Thus, the pixel size was reduced from 300μm to 200μm. According to Nyquist's criterion, the resolution of the obtaining images is approximately 400μm, compared to 600μm for the preexisting system. The beam fluence of the enhanced system appears to be significantly improved. The range of the fluence in the preexisting system is ranging from 75.22 mJ/cm^2 to 105.4 mJ/cm^2 while the values in the enhanced system are approximately one order of magnitude lower, ranging from 5.04 mJ/cm^2 to 15.00 mJ/cm^2. The SNR values of the two systems –in reference, of course, to the raw images– were also computed, in order to compare their sensitivity. The ratio of mean values of the enhanced over the preexisting system was 3, even though the laser fluence was considerably lower at the enhanced system. All the aforementioned differences are concisely shown in Table 1.

Table 1: Quantitative comparison of the two system versions

	Preexisting system	Optimized system
Maximum scan area of motorized stages (cm^2)	56.25	224
Scanning method	point–by–point	continuous
Acquisition time for a 3x3cm^2 area (mins)	200	75
Used pixel size (μm)	300	200
Transducer bandwidth (MHz)	100	11
Central frequency (MHz)	73	10
Beam fluence (mJ/cm^2)	(75.22, 105.4)	(5.04, 15.00)
SNR (average value)	12.84	39.34

4. Methods

4.1. Sample preparation

The initial samples for the proof of concept measurements of the original system, were made with mock–up murals, similar to the one presented in Fig. 30. Each sample has a geometric pattern or a plain drawing on the prepared gypsum substrate, coated with a thin layer of paint. For the creation of the samples, the gypsum is combined with a hardener and the mixture is placed in a Petri dish (usually not larger than 6cm in diameter) and left to dry for a couple of days. Then, the pattern that represents the hidden underdrawing of the mural is drawn, using a graphite pencil (Faber-Castell (B), Stein, Germany). Subsequently, one or two characteristic types of pigment are mixed with an acrylic binder (Lascaux Acrylic

Figure 30: Visual representation of a typical sample.

Adhesive 498 HV) and in some cases with gypsum, in order to form thick acrylic paints. Each paint paste was applied with the use of a paintbrush over the sketches, forming paint layers whose thickness was a few hundred µm. The pigments that were used for the samples are Ultramarine Blue, Chromium Green, Titanium White and Ochre Yellow. The majority of these samples were measured by the enhanced PA apparatus as well, both for the fine-tuning as well as for comparison reasons.

After the proof of concept measurements were realized, more realistic samples were scanned, with the collaboration of two different experimental teams from the National Institute of Optics, National Research Council (INO–CNR) and the University of Cagliari (UniCa). Fig. 31 presents the lateral view of the mock-ups provided by INO–CNR. These samples were specifically prepared, following the historical methodologies. Their support is composed of lightweight wood-fiber panel, while the arriccio and intonachino layers are composed of a mix slaked lime. In the lower layer, the mix is contains medium grained sand and water, while the upper layer is comprised of fine grained sand and water.

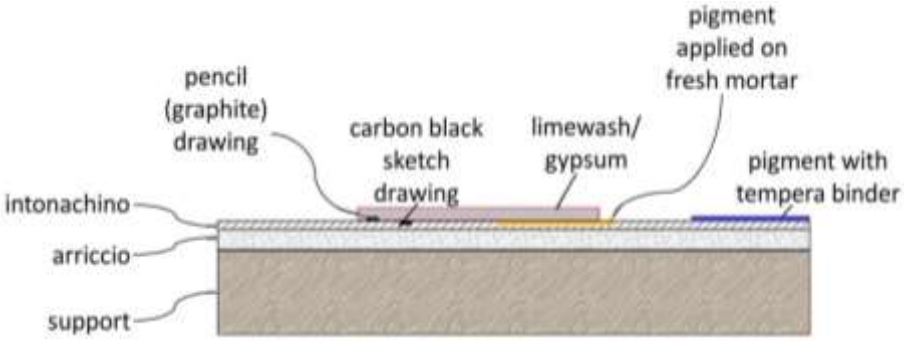

Figure 31: Stratigraphy of the mock-ups provided by INO-CNR.

The underdrawings, found on top of the intonachino layer, were made from different materials, like graphite, charcoal and sinopia. Finally, different parts of the samples were covered by layers of gypsum or limewash (a mixture of slaked lime in water which sets slowly by absorbing carbon dioxide from the air, with the addition of a small amount of milk) layers, or various pigments, like Egyptian Blue, Yellow Ochre and Raw Sienna. Each gypsum –or limewash– layer had an approximate thickness of 100 μm.

The final set of samples, contained both mural mock–ups and real murals –which originate to a fresco of the San Giuseppe Church in Cagliari, Sardinia, Italy–. This set of samples aimed

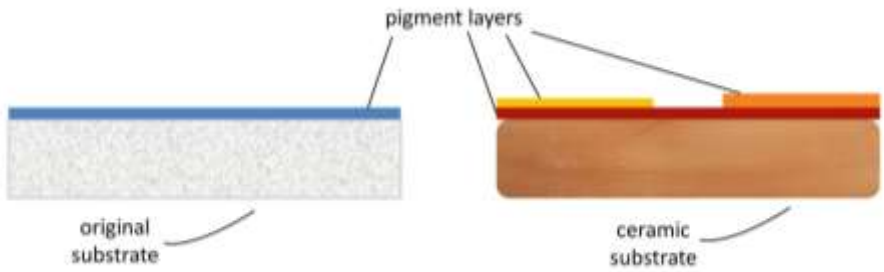

Figure 32: Stratigraphy of the mock-ups provided by the UniCa.

to investigate the ability of the PA system to measure the paint layers' thicknesses. The mock–ups were composed of two different substrates; the first ones had a substrate with a composition similar to the original murals, while the rest had a substrate made of a homogeneous ceramic layer (see section 5.2 for details). In each case, above the substrate was applied a different combination of pigments and numbers of layers. The pigments used for the creation of the samples, were Cadmium Yellow, Ochre, Cadmium Yellow, Cadmium Orange and Lapis Lazuli.

4.2. Acquisition

4.2.1. General information

In order to acquire the PA signal, the water–immersion transducer is submerged into the distilled water that fills the aluminum tank were the sample is attached. Afterwards, the position of the transducer is slightly altered, until the best possible focus is achieved. During each measurement, a square area of the sample –whose surface is defined by the user–, is being scanned. The scan begins when the top left corner of the area of interest is positioned below the transducer, and then, with the help of the motorized stages, the area of interest is raster scanned in a continuous way. When the measurement is completed, the sample returns to its original position, where the transducer is placed above the center of the selected area. The continuous way of the scanning, is a great enhancement in comparison to the preexisting system, where the acquisition was made point–by–point, and thus it was very time-consuming. In the developed system, the custom–made scripts calculate the maximum scan speed that the stages may reach for each measurement, by taking into account parameters such as the repetition rate (RR) of the laser, the selected scan area (Δx), the number of pixels (N_p), the number of averages (N_A) and also, the correction factor (a_{cor})

(see section 4.3 for details). The formula used for the calculation of the maximum scan speed is the following: $v_{max} = \frac{\Delta x}{N_p \cdot N_A} RR \cdot a_{cor}$ (55)

The transportation of the sample, therefore the movement of the stages, must happen in a very precise way, in order to prevent the blurring of the produced image. For this reason, an electronic controller is in charge of the synchronization of the trigger of the incident laser pulse, the movement of the stages and the acquired waveforms.

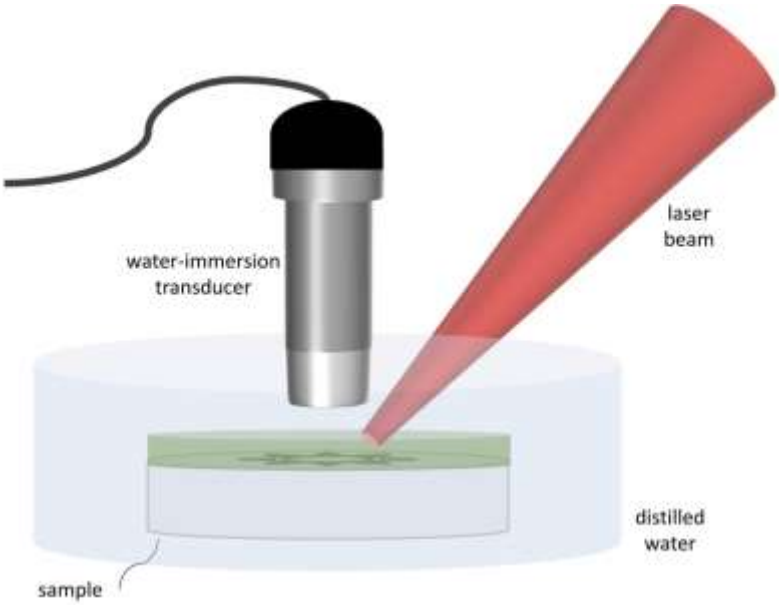

Figure 33: Visual representation of a sample being illuminated by the laser beam and the transducer being submerged into the distilled water, during the measurement.

4.2.2. Preparation of the agarose gels

In Section 5.3 the results of some measurements are shown, where the coupling medium of the transducer was altered, and instead of water, a combination of agarose gels was used. More information concerning the agarose is found in that section. In order to achieve the best possible results, two facts had to be kept in mind; first of all, in order to detect the produced ultrasounds, the transducer had to remain submerged into the agarose layer. Thus, the agar gel had to be fluid. On the other hand, in order to guarantee a good degree of water retention, the agarose gel that was in contact with the surface of the sample had to be solid. As a result, two subsequent layers –varying the agarose powder concentration in water, as well as its cooling conditions of agarose gel of different concentrations– were being placed over the samples. In the following paragraph the preparation of the agarose gels used during the experiment is described.

The first layer, which was in contact with the sample surface, was solid, while the second one was fluid and flexible. In both cases, the preparation is done in heating and cooling circles. The first layer, prepared by dissolving agar in distilled water at 2 wt%, was heated up to 90°C three times and cooled down under laboratory conditions (i.e. 25°C). During the last cooling cycle, at a temperature of around 35°C, the still fluid agarose gel was applied directly onto the wall painting surface to avoid any formation of air bubbles during jellification. The

second layer –prepared by dissolving agarose in distilled water at 0.25, 0.3, and 0.5 wt%– was heated up to 90°C two times and cooled down under laboratory temperatures, while stirring continuously. Upon reaching the laboratory temperature (25°C), the agarose gel, which maintained a fluid consistency due to stirring, was applied over the first –solid and protective– agarose layer. After comparing the acquired images with the aforementioned concentrations the formulation with 0.3 wt% was selected, which assured a constant immersion of the transducer during scanning movements and a stable in-place hold of the gel on the surface.

4.3. Data analysis

4.3.1. General information

In the preexisting system, the recorded waveforms are averaged in order to improve the signal to noise ratio (SNR), transferred to a computer where the signal is filtered, by cutting–off frequencies higher than 30MHz –for high frequency noise elimination– as well as frequencies lower than 100kHz, before the estimation of the peak–to–peak PA amplitude value. The initial unprocessed images were created using these peak–to–peak PA amplitude values. Regardless of the scanned area, the pixel size was kept constant to 0.3mm/pixel (e.g. for a 30x30mm^2 area, the obtained image is 100x100 pixels). For the acquisition of the PA image a MATLAB environment was used.

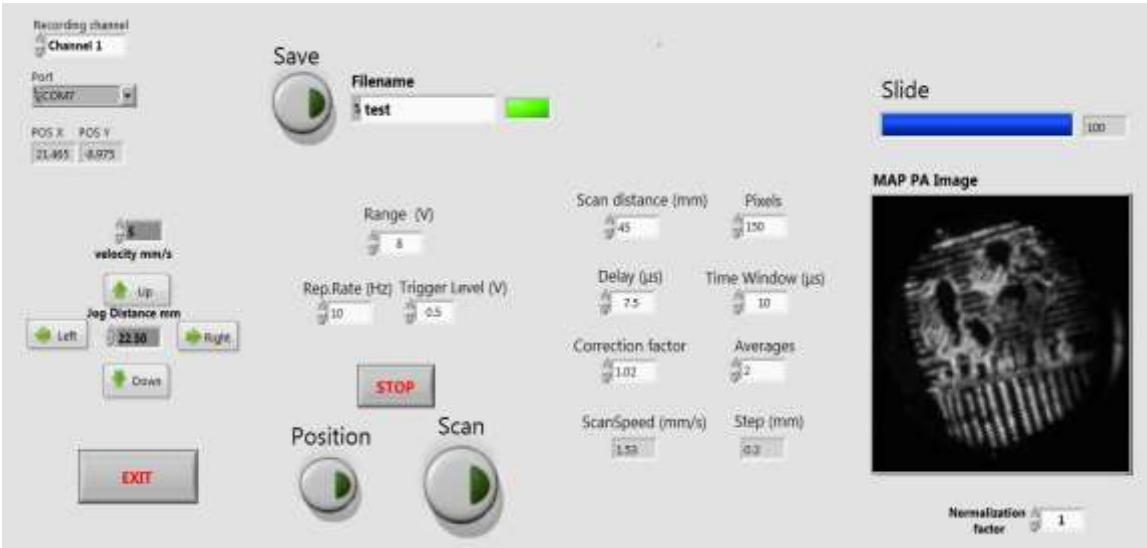

Figure 34: Screenshot of the user interface design used for the acquisition of the PA images.

In the enhanced system, the filtering of the signal is not necessary, since the sensitivity of the transducer is greatly improved. The pixel size of the acquired images of this system is also kept constant, but in this case the value is equal to 0.2mm/pixel.

As it is shown in Figure 34, the user may choose the parameters that best apply to the requirements of each sample. During the measurements that took place for the needs of this work, the values of the parameters were ranging from case to case. Some typical values are shown on Table 2.

Parameter explanation for Table 2: The time window represents the specific time domain that is being recorded by the system, in which lies the PA signal. The information that

appears in a single pixel of the final image is the result of the averaging of –at least– two PA signals. The temporal delay expresses the time needed for the ultrasound to traverse the distance between the underdrawing and the sensor of the transducer. The range of values (3.9–4.5) μs refers to the transducer used in the pre–existing, while the range of values (6.5–7.5) μs refers to the new one. The acquired points represent the number of points used to recreate the waveform, in the corresponding time window. The recording of the PA signal starts when the photodiode measures a signal which is equal or bigger than the value of the trigger level. The scan distance indicates the dimension of the area of interest, while the correction factor is a dimensionless number that is being multiplied by the scan speed and is responsible for the synchronization of the movement of the stages, the irradiation of the sample and the acquisition. When the correction factor is not used, the occurring images are blurry. This parameter was only used in the enhanced system, as the point by point acquisition was not affected by the scan speed. The last parameter (pixels) indicates the number of pixels found in one row of the created image.

Table 2: Typical values of the parameters

time window (μs)	2, 10, 20
number of averages	2, 4, 8
temporal delay (μs)	3.9 – 4.5, 6.5-7.5
acquired points	1000
trigger level (V)	0.5 – 2.5
scan distance (mm)	15 – 45
correction factor	1.02-1.022
pixels	50 – 150

4.3.2. Image processing

Apropos to the samples that contained underdrawings, the procedure that was followed in order to obtain the final contrast value is described below.

To begin with, the contrast (C) of each image was calculated, using the formula $C = \frac{A_{line} - A_{paint}}{A_{line} + A_{paint}}$ (56), where A_{line} and A_{paint} are the peak-to-peak PA amplitudes for graphite –or any other material used for the sketching of the underdrawings– and the overlying paint layer, respectively.

What is more, in order to get a more reliable value for the contrast of each sample, the values of the contrasts were derived as follows; five values of A_{graph} and A_{paint} were measured from adjacent areas of the sample, and for each pair, a contrast value was calculated, using Eq. 56. The average value of the five measurements is considered to be the final value of the contrast, which was used for the analysis.

Prior to the contrast calculation, the raw data was processed using ImageJ in order to reach the most eye pleasing results. The processing of the acquired images was different for each system. At the preexisting system, each image had its contrast enhanced by contrast

streching 0.3% of the total pixels, after the background noise was removed –using the command "Subtract background"–. The procedure followed in the enhanced system is described below. The use of the command "Despeckle" led to the smoothing of the lines of the underdrawings. After, the contrast was improved with the command "Non–linear means denoising". The resulting images are compared in Section 5.4.

The image processing of the INO–CNR samples (see results at Section 5.1.) included the contrast streching of 0.1% of the total pictures, both in the PA images and those acquired with NIR.

4.3.3. SNR calculation

Except for the processing procedures mentioned above, the SNRs of the raw images were computed. These calculations provided insight regarding the performance of the two systems as well as of the IR measurements, acquired with a filter at 1100nm. The SNR values that appear in this work are dimensionless numbers, computed using Eq. 57:

$SNR = \frac{A_{line}}{A_{noise}}$ (57), where, $\mathrm{A_{line}}$ is, again, the peak-to-peak PA amplitudes for graphite –or any other material used for the sketching of the underdrawings– and $\mathrm{A_{noise}}$ represents the value of the image noise and is computed from the standard deviation of the background values of the acquired image. In order to present more reliable results, the SNR value of every image presented in this project is the average value of five SNR measurements.

The SNR is a valuable tool for the sensitivity comparison between systems, as its values can be connected to the laser fluence; from Eq. 44 it is evident that the PA amplitude p_0 is proportional to the laser energy. What is more, an increase to the laser energy leads to a fluence increase. $\mathrm{A_{line}}$ corresponds to p_0 and thus is proportional to the laser energy, while the value of $\mathrm{A_{noise}}$ remains virtually constant, irrespective of the energy. As a result, if two systems produce raw images with comparable SNR values, while using completely different fluence values, the system using the lower fluence is much more sensitive, and ultimately, much more appealing to the heritage experts.

4.3.4. Depth profile creation and thickness calculation

As it has already been mentioned, the samples provided by the UniCa did not have any underdrawings. The aim of the measurements was to examine whether the PA effect could be used –in reflection mode– in order to study samples of complex stratigraphy and to measure the thickness of each layer. The idea is based on the fact that ultrasounds, contrarily to light, are traversing relatively short distances in an easily measured time, and thus, the ultrasounds created in the different layers of the sample (whose thickness is ranging from approximately 50μm to a few hundred μms) can be detected separately. An equivalent procedure was followed in the transmission configuration example that was presented in 1.3.7. In order to acquire the desired cross-sections, the custom–made scripts had to be altered. In this case, the entirety of the PA waveform was being recorded, since the peak–to–peak values do not provide the necessary information. The data was saved in binary format. After the acquisition, with the use of Matlab, the binary files recreated consecutive images. With the help of ImageJ a stack of images was created, where each slice

corresponded to a different depth. By taking into consideration the time between two adjacent acquired points of the waveform, and considering the fact that the velocity of the ultrasounds is 1498m/s (at 25°), the distance between two consecutive slices can be calculated. Finally, with the use of an ImageJ plugin, namely 3D Volume Viewer, the stratigraphic column of the sample is created. In order to compute the average depth of each layer, 20 depth profiles were collected from each sample. From each depth profile, a 1D array of intensities in relation to depth (z-axis) was extracted and plotted at an I(z)–z diagram. The peaks appearing at the graph due to every existing layer were fitted with a Lorentzian distribution function. The thickness of the corresponding layer was calculated from the full width at half maximum (FWHM) of each curve. For greater accuracy, the final estimation of the thickness of each payer was calculated by the average value of the 20 acquired FWHM. The standard deviation of the FWHM measurements was considered the as the error for every average estimation. Signals coming from depths larger than 1mm were not included into the depth maps, since they were considered reflections of other PA signals.

In some samples, multiple PA signals with the same trend, but a decrease in intensity appear to exist. This condition could be associated to reflection or/and scattering phenomena occurring due to the inhomogeneity of the substrate of those samples. As a matter of fact, the substrates of the fresco fragments were composed of sand grains of variable sizes, which could indeed produce these spurious PA signals. To verify this assumption, and to understand whether these signals feebler signals had to be excluded from the creation of the cross section of the samples, two different morphologies of fresco mock-ups were reproduced: the substrates of the first kind had substrates similar to the original (sand, calcium hydroxide, calcite), while the second one had a homogeneous substrate of compact earthenware. Both the mentioned typologies were realized with different painting structures.

5. Results

The results of the experiments are presented in the following sections. They are divided into five parts. In most cases, the data was collected with the use of the preexisting system. These measurements provided useful feedback which led to the enhancment of the current system.

5.1. PAI in realistic mock-ups (INO-CNR Samples)

The first set of samples that were measured for the needs of this project, were realistic mock–ups of murals, on which different grounds and drawing methods were used. The PA images were aquired with the preexisting system. Below, the prosseced PA images are compared to photographs taken using NIR at 1050nm, at INO–CNR. In these measurements, the efficacy of the system was put to test on different cases of drawing methods. The results are presented in Fig. 35–41.

The underdrawing in sample 1.1, which is covered with a 70μm thick blue tempera layer (Egyptian Blue) applied with egg tempera binder, represents a city skyline drawn mostly with graphite, except for the line at the top left which was drawn with charcoal, was visualized

more successfully with the NIR than with the PAI system. Nevertheless, the PA image clearly reveals the sketch drawing made with graphite on the dried mortar. The charcoal line cannot be detected with the PAI system due to the different absorbing coefficients the two materials have at 1064nm (the laser irradiation wavelength). The graphite absorbs a significantly much larger percentage of the radiation in relation to the charcoal. Since the contrast is proportional to the absorption coefficient and also relative to the scanned area, feebler PA signals, like those produced from the charcoal, are not visible.

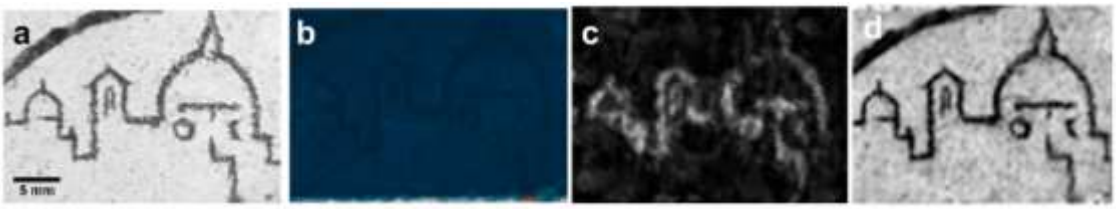

Figure 35: Sample 1.1.; Charcoal and graphite underdrawings hidden under Egyptian Blue tempera paint. (a) underdrawing prior to the paint application, the line on the upper corner is drawn with charcoal the rest is drawn with graphite (visible image) (b) secco overpaint (after the application of the tempera)–the underdrawing is slightly visible to the naked eye– (c) PA image (d) NIR image at 1050nm.

The underdrawings of samples 1.2 and 1.3 are composed of charcoal and sinopia. The sketches are covered with limewash. Sample 1.2 has a single layer of limewash, while sample 1.3 is divided in two areas with different numbers of layers; the left side has only a single layer of limewash, while the right side consists of two layers. The thickness of the single layer is approximately 60µm, whereas the right side of sample 1.3 is covered by a 140µm limewash layer.

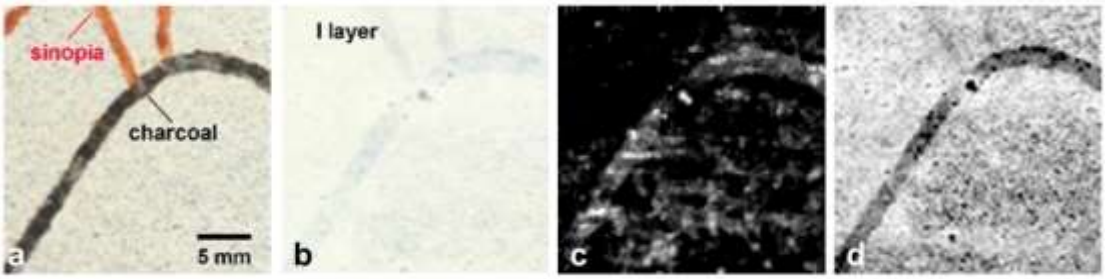

Figure 36: Sample 1.2; Charcoal (dark gray) and sinopia (red) underdrawings hidden under a single layer of limewash. (a) underdrawing prior to the limewash application (visible image) (b) after the limewash cover–the underdrawing is slightly visible to the naked eye– (c) PA image (d) NIR image at 1050nm.

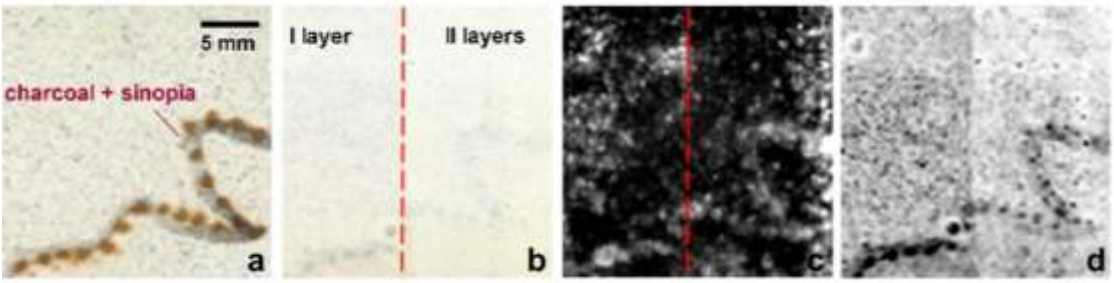

Figure 37: Sample 1.3; Charcoal (dark gray) and sinopia (red) underdrawings hidden under a single (left side) and two layers (right side) of limewash. (a) underdrawing prior to the limewash application (visible image) (b) after the limewash cover–the underdrawing is slightly visible to the naked eye on the left side– (where the single layer covers the underdrawing) (c) PA image (d) NIR image at 1050nm.

The NIR photo depicts the underdrawings of both materials, while the PAI only detects the charcoal. Nevertheless, the PAI presents a higher contrast value for sample 1.2 (with a view to the charcoal line) compared to the NIR. The ratio of the contrast values of the PA over the NIR is 1.28. The contrasts of sample 1.3 though, are even closer for the two images; this time, the ratio is 1.08.
In the previous two cases, the PAI technique outweighs the NIR apropos to the contrast of the charcoal. On the other hand, the NIR is able to depict the sinopia underdrawings, contrarily to the PAI.

Samples 1.4 and 1.5 have underdrawings composed of charcoal and sinopia as well, but this time the covering layers are made from gypsum. Sample 1.4 has a single gypsum layer over the underdrawing, with approximately 80µm thickness, while sample 1.5 has a double covering layer, with a thickness equal to 190µm.

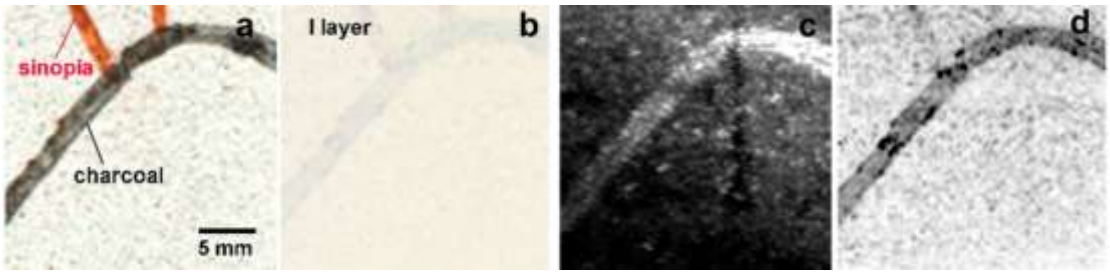

Figure 38: Sample 1.4; Charcoal (dark gray) and sinopia (red) underdrawings hidden under a single gypsum layer. (a) underdrawing on the substrate prior to the application of the gypsum (visible image) (b) after the gypsum coat –the underdrawing is slightly visible to the naked eye– (c) PA image (d) NIR image at 1050nm.

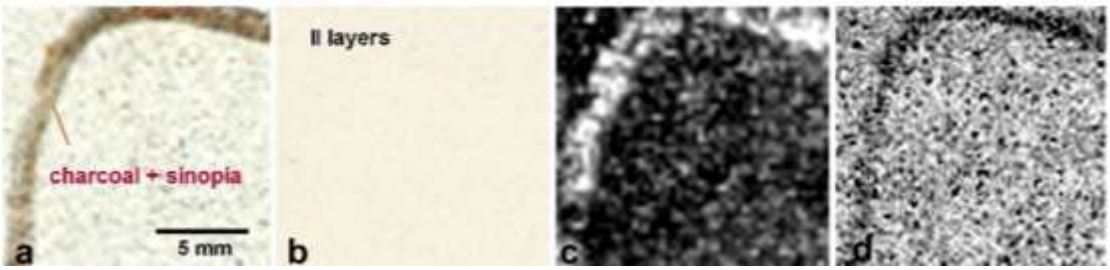

Figure 39: Sample 1.5; Charcoal (dark gray) and sinopia (red) underdrawings hidden under two gypsum layers. (a) underdrawing on the substrate prior to the application of the gypsum (visible image) (b) after the gypsum coat – the underdrawing is not visible to the naked eye– (c) PA image (d) NIR image at 1050nm.

The contrast of the two samples is, in both cases, better in the PA images. The ratio of the PA contrast over the NIR is 1.62 and 2.47, respectively. This result, though, refers to the charcoal underdrawing. The sinopia lines found at the top side of sample 1.4 are feebly visible only to the NIR image [Fig. 38d].

The next sample has underdrawings composed of charcoal and sinopia, which are firstly covered with a layer of Egyptian Blue fresco paint and after, with a thick gypsum layer, with an approximate thickness of 80µm. Again, the charcoal line was detected with both imaging techniques, while the sinopia underdrawings were not visible with PAI.

The last sample of this section, has a charcoal underdrawing that is initially covered with Raw Sienna fresco paint and then, with a limewash layer. The thickness of the last layer is approximately 70µm. The resulting images show that the PAI can depict the charcoal line

decently. On the other hand, the NIR photo at 1050nm cannot distinguish the line under the Raw Sienna and gypsum layers, possibly due to the absorbance of a critical amount of light in these depths.

Figure 40: Sample 1.6; Charcoal (dark gray) and sinopia (red) underdrawings hidden under fresco paint and gypsum coat. (a) underdrawing on the substrate prior to the application of the paint and gypsum (visible image) (b) after the application of the Egyptian Blue (fresco paint) (c) after the gypsum coat –the underdrawing is not visible to the naked eye– (d) PA image (e) NIR image at 1050nm.

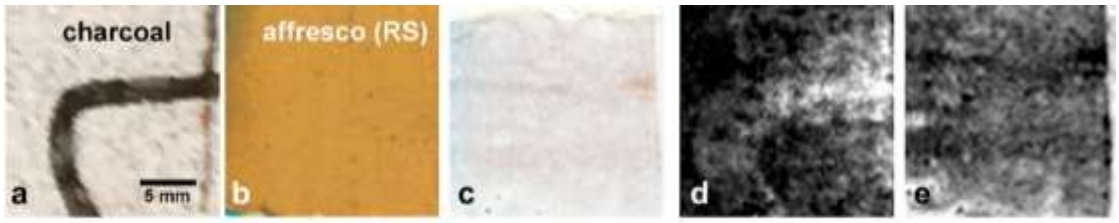

Figure 41: Sample 1.7; Charcoal underdrawing hidden under fresco paint and limewash coat. (a) underdrawing on the substrate prior to the application of the paint and gypsum (visible image) (b) after the application of the Raw Sienna (fresco paint) (c) after the gypsum coat –the underdrawing is not visible to the naked eye– (d) PA image (e) NIR image at 1050nm.

It is interesting to notice that in the last two cases the lines of the charcoal underdrawings appear to be spread, compared to the original sketches [Fig. 40d, 41d]. A reasonable explanation for this result is the fact that when these lines were drawn, the mortar was still damp, because these samples were meant to imitate the fresco execution method. The existing moist at the substrate led to the dispersion of black pigment particles. This information cannot be derived with the NIR technique.

5.2. PAI for stratigraphy analysis (UniCa Samples)

The second set of samples that was measured with the preexisting experimental apparatus comprised of the samples provided by the UniCa. During the processing of the samples a peculiar behavior was noticed in the samples originating from San Giuseppe Church [Fig. 42]; in the extracted stratigraphic profiles there seemed to be a lot more layers than expected. The exact number of layers was known due to measurements realized with Spatially Off-set Raman Spectroscopy (SORS). In order to understand the newly acquired data, the mock-up samples were measured as well. The results were very promising since, after the processing, the expected stratigraphic profile was revealed. The following figures [43-45] juxtapose the transverse profiles of the samples which were acquired with the foresaid

Figure 42: Part of the fresco in San Giuseppe church.

methods. The dimension of the z-axis is stretched in order to visualize the stratigraphy more clearly.

The first three samples are frescos from San Giuseppe Church. Sample 2.1 consists of 3 painted regions, and each one consists of 3, 2, and 2 layers of paint respectively. The upper layers, consist of amorphous carbon black (graphite) mixed with calcite, the intermediate layer has a brown/gray color and is composed of a mixture of calcite, graphite, hematite and gypsum. The last one is a mixture of hematite, calcite, calcium and gypsum. Sample 2.2 consists of a single layer. The pink color is obtained by mixing hematite (red), graphite (black) and gypsum (white). In sample 2.3 only the middle area was analyzed (the brown/gray area). Its composition is the same with the upper layer of sample 2.1. The PA depth profiles presented at Fig. 43-45c do not contain the pieces were the reflections appeared. What is more, the z-axis is oriented from the right to the left side of the depth profiles.

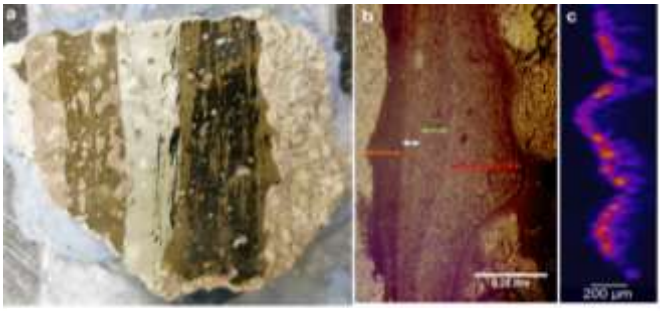

Figure 43: Sample 2.1; a) lateral view of the mural fragment b) SEM image of the stratigraphy of the sample. The orange, white and green arrows indicate the first, second and third layer respectively. The red arrow indicates the substrate. c) final PA depth profile, composed of approximately 400 slices.

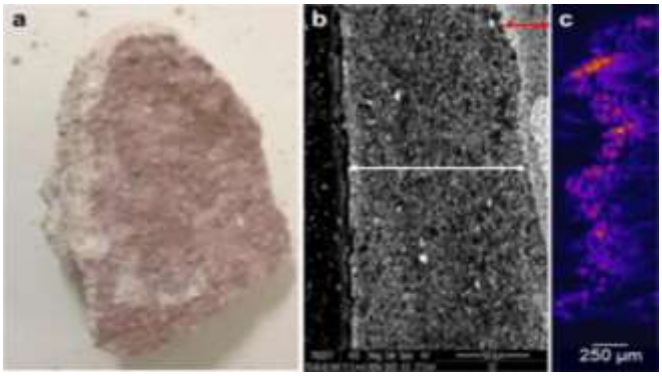

Figure 44: Sample 2.2; a) lateral view of the mural fragment b) SEM image of the stratigraphy of the sample. The white arrow indicates the paint layer. The red arrow indicates the substrate. c) final PA depth profile, composed of approximately 300 slices.

The correct selection of the part with the correct signals was accomplished with the use of the information acquired from Fig. 46-49. In these figures, the PA profiles of the mock-up samples are shown. These had a pivotal significance for the better understanding of the profiles of the real murals. As it has been mentioned before, two of the samples (2.4 and 2.5) had a substrate similar to the substrate of the samples from San Giuseppe, while the rest (samples 2.6 and 2.7) had a smooth, ceramic substrate.

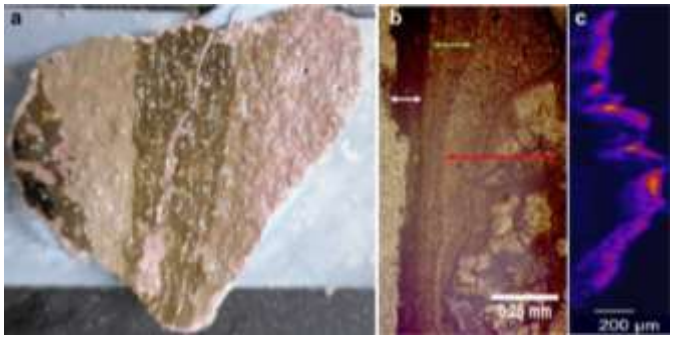

Figure 45: Sample 2.3; a) lateral view of the sample b) SEM image of the stratigraphy of the sample. The white and green arrows indicate the first and second layer respectively. The red arrow indicates the substrate c) final PA depth profile, composed of approximately 400 slices.

Figure 46: Sample 2.4; Lime, sand and calcium hydroxide substrate with a cover layer of Lapis Lazuli. From left to right: A photograph of the surface area of the sample, a visual representation of the depth profile and the recreation of the cross-section of the cover layer with the acquired PA data.

Figure 47: Samples 2.5; Lime, sand and calcium hydroxide substrate with a cover layer of Cadmium Orange. From left to right: A photograph of the surface area of the sample, a visual representation of the depth profile and the recreation of the cross-section of the cover layer with the acquired PA data.

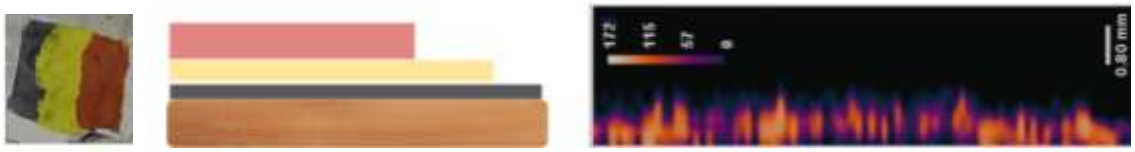

Figure 48: Sample 2.6; Ceramic substrate with covered by three layers, consisting of Graphite, Cadmium Yellow and Ochre (moving from the lower to the upper layer). From left to right: A photograph of the surface area of the sample, a visual representation of the depth profile and the recreation of the cross-section of the cover layer with the acquired PA data.

Figure 49: Sample 2.7; Ceramic substrate with covered by three different combinations of layers, the first one consists of Ochre and Cadmium Yellow the second one is only composed of Ochre and the last one is made of Ochre and Cadmium Orange. From left to right: A photograph of the surface area of the sample, a visual representation of the depth profile and the recreation of the cross-section of the cover layer with the acquired PA data. The recreation corresponds to the area between the yellow and orange layers, where the ochre is visible at some spots. The regions with the higher signals correspond to the areas where the ochre is uncovered.

With the insight provided by these mock-ups, it was possible to distinguish the useful parts of the signals, for the recreation of the depth profiles. The results of the depth estimations are presented in the following table, along with the measurements acquired with SORS, which is a technique widely used for the this purpose.

Table 3: layer thickness comparison (PA and SORS)

	PA measurements			SORS measurements		
Figure number	Layer 1 (μm)	Layer 2 (μm)	Layer 3 (μm)	Layer 1 (μm)	Layer 2 (μm)	Layer 3 (μm)
43	60 ± 15	71 ± 20	137 ± 30	81 ± 30	60 ± 20	92 ± 30
44	133 ± 20	-	-	107 ± 50	-	-
45	70 ± 20	85 ± 20	-	80 ± 30	61 ± 20	-

In general, the depth estimations of the two methods are in convergeance, and lie inside the limits of the statistical errors that occurred during the analysis. The importance of the results though, is great, since they give rise to new applications of the PAI technique.

5.3. Agarose gel as a coupling medium (INO-CNR Samples)

After testing the system in different kinds of samples and obtaining knowledge of its capabilities, its major drawback, the water usage as a coupling medium, had to be faced in order to make it more appealing to heritage experts. For this reason, agarose gel was introduced as a non-destructive medium.

Agarose is a natural polymer prepared from seaweed (red algae) and consists of the D-galactose and 3,6-anhydro-L-galactose repeating units. Agarose can be dissolved in boiling water and a gel is formed after cooling this solution below 45 °C, as a result of extensive hydrogen-bonding between the agarose chains. The gelling temperature may vary due to monomer composition and concentration of the solution and may also be altered by chemical derivatization of the polymer. Agarose gel is widely used in various conservation treatments on cultural heritage objects, and it has been proven to be safely applicable on delicate surfaces.

In the following figures is shown the effectiveness of the system when agarose gels are used as the coupling medium for the propagation of the ultrasonic waves. The results are compared with images of the same samples, acquired using water as the coupling medium. All the measuring parameters were kept the same, in order to have a consistent way to compare the results. What is more, the processing of the images was the same for each couple of images (c, d), in order to extract reliable conclusions.

The first three samples [Fig.50-52] have already been described in section 5.1. It is evident that in all cases, the acquisition with water as the coupling medium produces more elegant results. The images acquired in agarose appear to have an artefact, where in every two adjacent rows the intensity of the signals is fluctuating.

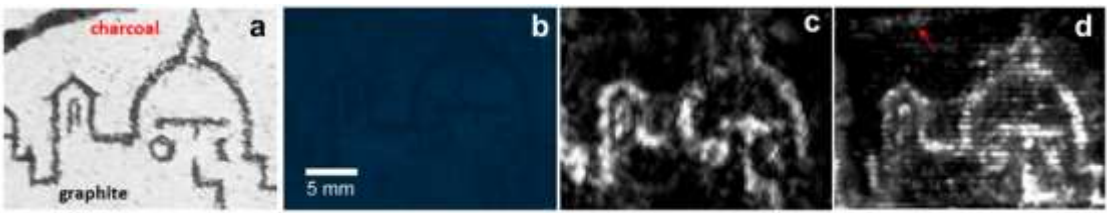

Figure 50: Sample 3.1.; Charcoal and graphite underdrawings hidden under Egyptian Blue tempera paint. (a) underdrawing prior to the paint application, the line on the upper corner is drawn with charcoal the rest is drawn with graphite (visible image) (b) secco overpaint (after the application of the tempera)–the underdrawing is slightly visible to the naked eye– (c) PA image where water was used as the coupling medium (d) PA image where agarose gel was used as the coupling medium. The red arrow points out the charcoal line that was detected in this case.

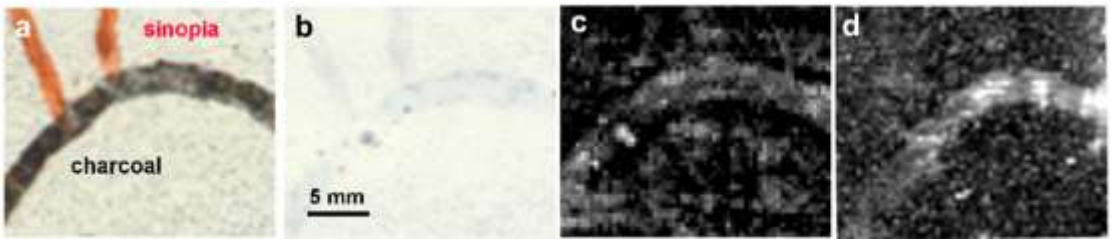

Figure 51: Sample 3.2.; Charcoal (dark gray) and sinopia (red) underdrawings hidden under a single limewash coat. (a) underdrawing prior to the limewash application (visible image) (b) after the limewash coat –the underdrawing is slightly visible to the naked eye– (c) PA image where water was used as the coupling medium (d) PA image where agarose gel was used as the coupling medium.

The ratio of the contrast values of the paired measurements, are equal to 1.1, 1.2 and 0.57, respectively. The result of sample 3.3 is particularly promising, since the average contrast of the image acquired in agarose appears to be almost double to the one acquired in water. Also, it is interesting to point out the fact that in the first sample, the agarose measurement might be able to provide information about the charcoal line on the top left corner of the image (shown with the red arrow). The PA signal is low and the line is not depicted in its entirety, but it is probable that it is indeed detected by the transducer. The two following samples have the limewash and gypsum covers, respectively. In both cases, the PAI systems fail to detect the sinopia lines, due to the fact that the material does not absorb sufficiently at the illuminating wavelength.

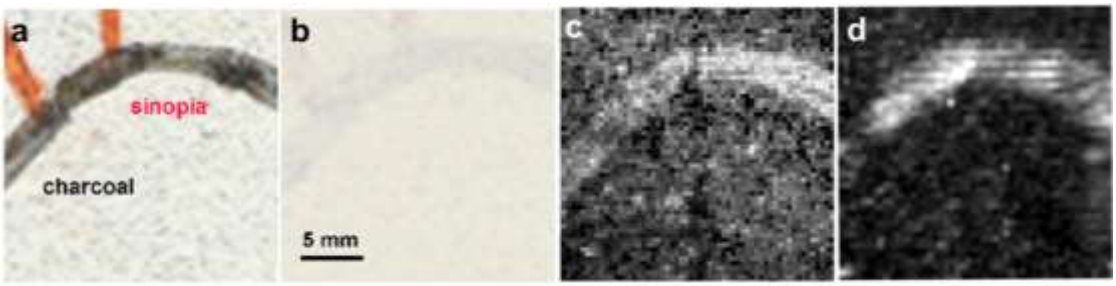

Figure 52: Sample 3.3.; Charcoal (dark gray) and sinopia (red) underdrawings hidden under a single gypsum layer. (a) underdrawing prior to the gypsum application (visible image) (b) after the gypsum cover –the underdrawing is slightly visible to the naked eye– (c) PA image where water was used as the coupling medium (d) PA image where agarose gel was used as the coupling medium.

Sample 3.4 consists of charcoal and sinopia underdrawings that are covered by a total of two paint layers. The application is done following out fresco painting techniques and the applied paint is Yellow Ochre. On top of the paint layers, a final layer of shellac varnish was spread.

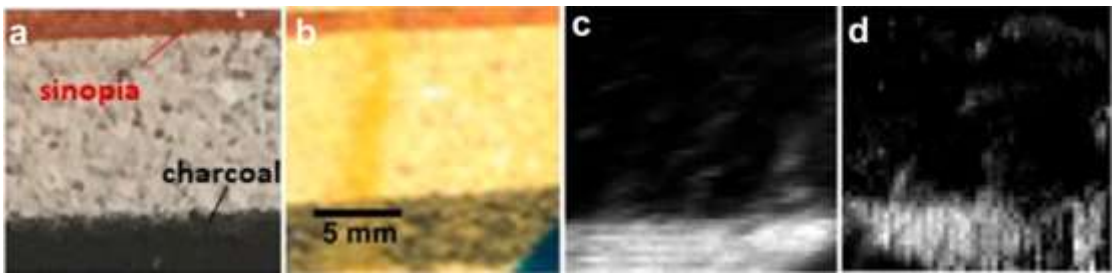

Figure 53: Sample 3.4.; Charcoal (dark gray) and sinopia (red) underdrawings hidden under two layers of Yellow Ochre fresco paint. On top of the paint layers a layer of varnish was added (namely, shellac). (a) underdrawing prior to the application of the paint layers (visible image) (b) after the application of the paint and shellac–the underdrawing is visible to the naked eye– (c) PA image where water was used as the coupling medium (d) PA image where agarose gel was used as the coupling medium.

Sample 3.5 consists of charcoal and sinopia underdrawings that are covered by a total of four consecutive paint layers. The bottom two are done by following out fresco painting techniques and the applied paint is Yellow Ochre, while the other two layers consist of Egyptian Blue tempera. On top of these layers, a final layer of shellac varnish was spread.

Sample 3.6 also consists of charcoal and sinopia underdrawings that are covered by three Egyptian Blue fresco paint layers. In this sample, the shellac varnish coating was not applied.

From Fig. 53–55, it can definitely be said that the detectability of the underdrawings of fresco and secco paintings is clearer when water is used as the coupling medium. This could

be related to the incomplete adherence of the first agar gel layer to the varnished or unvarnished samples, to the rough pigmented surface and to the consequent presence of small air gaps. The latter can compromise the detectability of the PA signal.

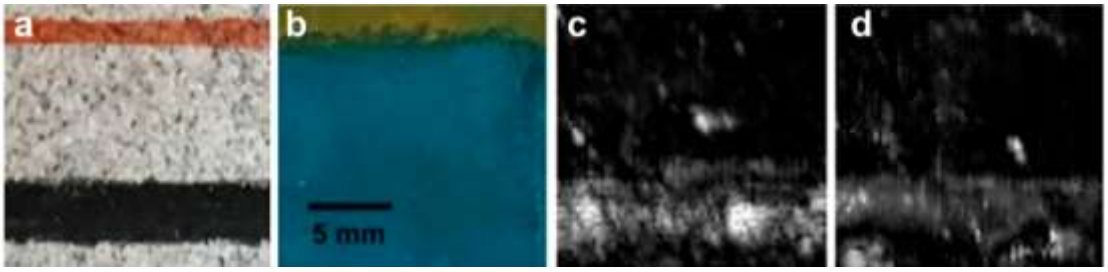

Figure 54: Sample 3.5; Charcoal (dark gray) and sinopia (red) underdrawings hidden under four (2+2) layers of Yellow Ochre (fresco paint) and Egyptian Blue (tempera). On top of the paint layers a layer of varnish was added (namely, shellac). (a) underdrawing prior to the application of the paint layers (visible image) (b) after the application of the paints and shellac–the underdrawing is not visible to the naked eye– (c) PA image where water was used as the coupling medium (d) PA image where agarose gel was used as the coupling medium.

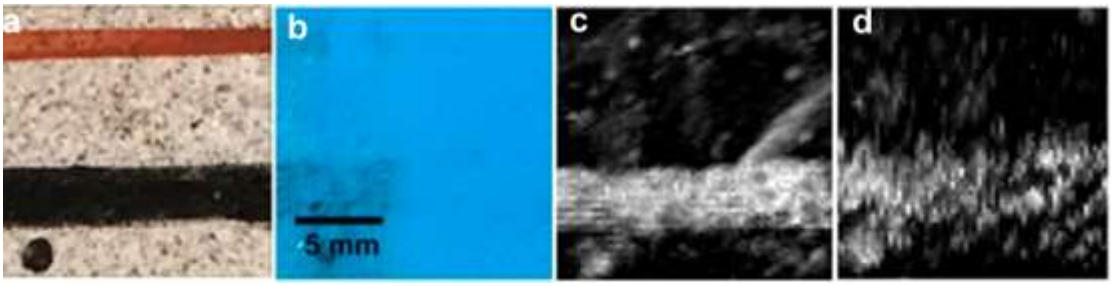

Figure 55: Sample 3.6; Charcoal (dark gray) and sinopia (red) underdrawings hidden under three layers of Egyptian Blue fresco paint. (a) underdrawing prior to the application of the paint layers (visible image) (b) after the application of the paint –the underdrawing is not easily visible to the naked eye– (c) PA image where water was used as the coupling medium (d) PA image where agarose gel was used as the coupling medium.

The ratio of the contrast of these measurements for each of the three samples is 1.04, 0.98, and 1.01. Therefore, the performance of the two methods in these cases apropos to the contrast is, practically speaking, the same.

In conclusion, the strongly absorbing features, i.e., charcoal lines, are revealed both in water and in agar, in the presence of one up to four hiding paint layers or one gypsum/limewash coat. Furthermore, the detectability of all the charcoal lines, either in water or in agar, is compromised by the upper coat of shellac varnish.

5.4. Image quality comparison between the two versions of the PAI system

All the foresaid results provided us with useful insight, which resulted into the quantification of the observations made during the measurements. Hence, the lab proceeded to specific purchases which led to the new, optimized PAI system. In this section, a qualitative comparison between the two versions of the PAI system takes place, following on from section 3.2. The samples that are presented here are the least realistic apropos to the procedures followed during their creation, and the materials used as grounds. The purpose of these measurements was to examine whether the newly enhanced system was functioning properly, and also to provide insight about the improvements that were made to the original experimental apparatus.

As it has already been mentioned in section 1.3.2., NIR is a technique broadly used in diagnostics of artworks. In order to prove the importance of the current work, images of the underdrawings of the samples were obtained with the MSI system of the IESL (IRIS-II) as well, in a spectral range between 1000–1200nm, with a view to comparing the two methods as well. In most cases, the contrast of the PA was higher than the one obtained by the IR. In each of the following figures are shown (a) the underdrawing prior to its cover with paint (sometimes mixed with gypsum) layers, (b) the image of the finished sample, (c, d) the PAI acquisitions from both versions of the system and finally and (e) the respective NIR image at 1050nm.

The first two samples [Fig. 56a–57a] are composed of a graphite underdrawing covered by three and four Titanium White paint layers, respectively. The sides of the PAI images 56c and 57c are 2cm, while the side of images 56d and 57d is 3cm.

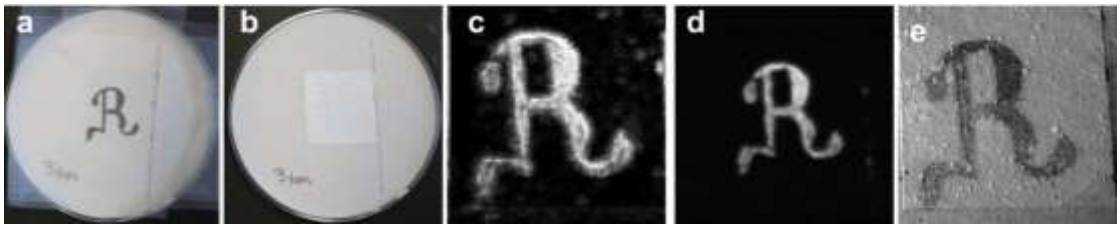

Figure 56: Sample 4.1; Graphite underdrawings hidden under four layers of Titanium White paint (a) Photo of the underdrawing prior to the overpainting (visible image) (b) Photo of the sample after the application of the paint (c) PA image acquired with the preexisting system (d) PA image acquired with the enhanced system (e) NIR image at 1050nm.

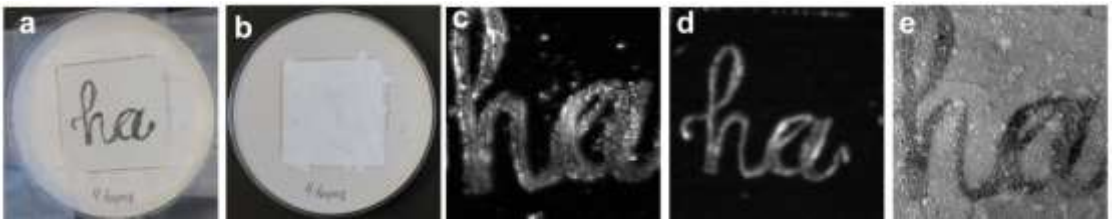

Figure 57: Sample 4.2; Graphite underdrawings hidden under three layers of Titanium White paint (a) Photo of the underdrawing prior to the overpainting (visible image) (b) Photo of the sample after the application of the paint (c) PA image acquired with the preexisting system (d) PA image acquired with the enhanced system (e) NIR image at 1050nm.

Next, a sample composed of graphite underdrawings covered by three layers of Ultramarine Blue paint is presented. The measuring surface area in all cases was 9cm^2.

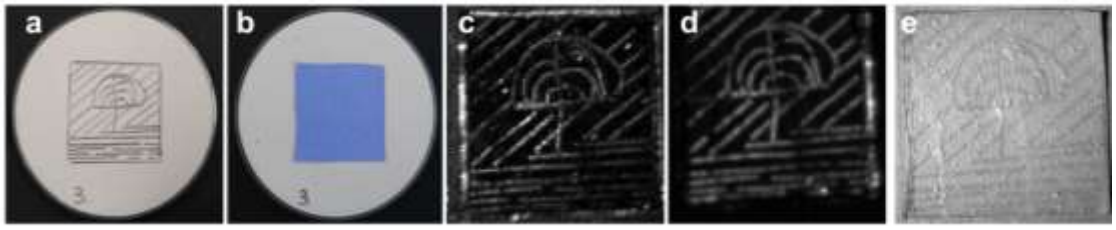

Figure 58: Sample 4.3; Graphite underdrawings hidden under three layers of Ultramarine Blue paint (a) Photo of the underdrawing prior to the overpainting (visible image) (b) Photo of the sample after the application of the paint (c) PA image acquired with the preexisting system (d) PA image acquired with the enhanced system (e) NIR image at 1050nm.

Sample 4.4 has a graphite underdrawing which is covered by three layers of Ochre Yellow and Titanium White paints. The measuring surface area was 900mm^2 in each case.

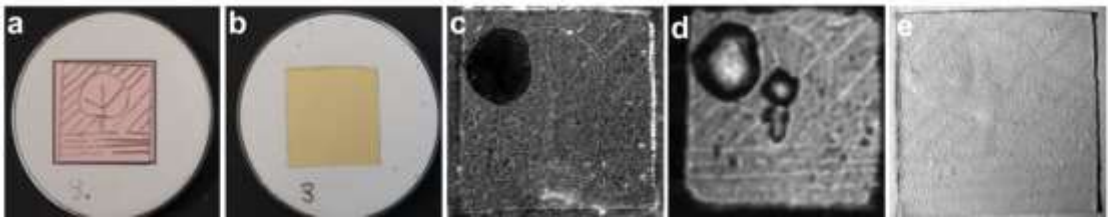

Figure 59: Sample 4.4; Graphite underdrawings hidden under three layers of a combination of Yellow Ochre and Titanium White paint (a) Photo of the underdrawing prior to the overpainting (visible image) (b) Photo of the sample after the application of the paint (c) PA image acquired with the preexisting system (d) PA image acquired with the enhanced system (e) NIR image at 1050nm.

The PAI of this particular sample stand out, due to an unexpected apparition. In Fig. 59c and 59d one can easily notice a round shape that appears on the top left corner of the images. It may seem unfortunate that the underdrawings behind this round formation cannot be depicted, though the heritage experts could extract another piece of information from these images; the existence of air, trapped between the substrate and the paint layers, also known as "detachment". As it has been mentioned before, the ultrasounds attenuate much faster in air. As a result, the air bubble that is trapped crucially decreases the signal amplitude, and the transducer does not detect the created PA wave. The two images (Fig. 59c, d) were acquired at different time periods. During the interim, a new detachment emerged, which can easily be observed at the center of Fig. 59d. A difference between these two images is that in the second case, the created bubbles are depicted as dark outlines with bright signals at the middle, while in the first case, the signal coming from the area of the bubble is homogeneous and very low.

Sample 4.5 is composed of a graphite underdrawing covered by four layers of Chromium Green paint mixed with gypsum. The scanned area was 6.25cm^2 and 9cm^2, respectively for images 60c and 60d.

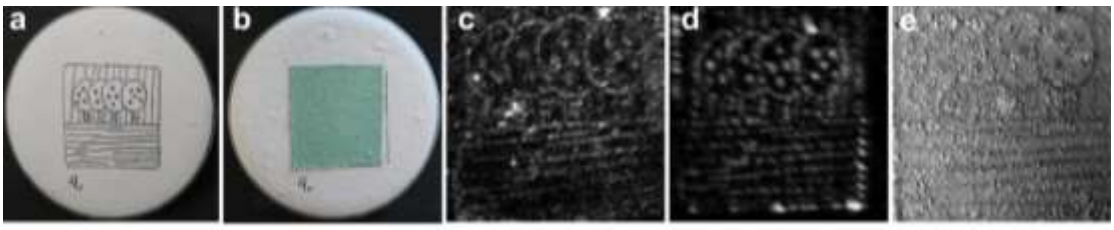

Figure 60: Sample 4.5; Graphite underdrawings hidden under consecutive layers of Chromium Green paint mixed gypsum (a) Photo of the underdrawing prior to the overpainting (visible image) (b) Photo of the sample after the application of the paint and gypsum mix (c) PA image acquired with the preexisting system (d) PA image acquired with the enhanced system (e) NIR image at 1050nm.

It should be underlined that the two versions of the PAI system are not limited by the artefacts of the surface of the samples –such as the undissolved gypsum that is present into the paint layer– in the same degree with the NIR photos, where each formation degrades the image quality.

The last mock-up presented in this section, presented in Fig. 61, consists of graphite underdrawings that are covered by a mixture of Ultramarine Blue and gypsum. The scanned area in both PAI cases was 20.25cm^2.

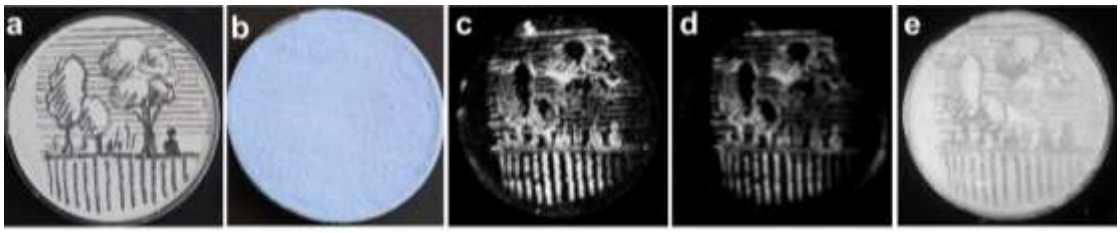

Figure 61: Sample 4.6; Graphite underdrawings covered with consecutive layers of Ultramarine Blue paint mixed gypsum (a) Photo of the underdrawing prior to the overpainting (visible image) (b) Photo of the sample after the application of the paint (c) PA image acquired with the preexisting system (d) PA image acquired with the enhanced system (e) NIR image at 1050nm.

The quantitative results for all the samples are gathered in the following table. The calculations were excecuted as described in section 4.3.2. The thickness of the samples has been measured during the previous project, with the use of a profilometer. The comparison of the imaging systems and techniques are presented in Table 4.

Table 4: Thicknesses and contrasts of the samples

Figure number	Thickness (μm)	PAI_1 (preexisting) contrast	PAI_2 (enhanced) contrast	IR contrast	Contrast Ratio (PAI_2/PAI_1)	Contrast Ratio (PAI_2/IR)
56	150	0.95	0.93	0.22	0.98	5.31
57	200	0.93	0.84	0.19	0.91	4.33
58	246	0.91	0.92	0.13	0.89	6.10
59	222	0.18	0.20	0.082	1.13	2.51
60	257	0.74	0.82	0.27	1.11	3.01
61	-	0.80	0.81	0.21	1.15	4.35

After observing the results shown in Table 4, a number of conclusions can be extracted with certainty. First of all, the contrast ratios of the sample set, proves that the enhanced system has a much better performance in comparison to the old system. The value of the ratio is in most cases very close to 1 –ranging from 0.89 to 1.15–. The key-point here is to remember the fact that the PA images acquired with the enhanced system have not undergone contrast stretching on purpose, conversely to those acquired with the old apparatus. Also, the fluence values used in each case were very different, with those used in the preexisting system being approximately five times higher. Thus, the contrast ratio values fluctuations around 1 prove the increased efficiency and the potential of the optimized apparatus. What is more, the fact that the ratio PAI_2/IR is greater than 1 was partially expected, due to the results of a previous project, where the proof of concept of the preexisting PAI apparatus in reflection configuration had taken place. The contrast ratio of the optimized PAI system over the NIR is ranging from 2.5 to 6.1, depending on the sample.

5.5. Other projects

Before the enhancement of the PAI apparatus, the transmission configuration was used for a couple of projects. The apparatus consisted of a spherically focused, non-contact transducer (NCT1-D7-P10, The Ultran Group, State College, PA, USA; nominal central frequency: 1 MHz; focal distance: 10 mm; numerical aperture: 0.31) and a holder specifically designed for its geometry. The rest of the apparatus was unchanged. The only noteworthy difference was

Figure 62: PAI in transmission configuration.

the fact that the illumination of the samples happens at its rear side, while the ultrasonic transducer is placed in the front side of the sample, as seen in Fig. 62. Below two case studies are presented, where the capabilities of the PAI system in transmission configuration were investigated. The first case –which is presented right after this introduction– is also the first recorded application of PAI on a real historical painting.

5.5.1. PAI measurements on a historical painting

The first project is a case study of a real historical painting [Fig. 63], aiming to test the potential of PA methods for the analysis of paintings. The artwork is an autograph nineteenth-century oil-painting on canvas (surface area: 16×22 cm^2), of private ownership. The painting has a double canvas due to a restoration operation called "lining", where an additional fabric is attached on the backside of a deteriorated textile support, aiming to strengthening it. The lining has been applied on paintings since the 18th century, making use of wax-based adhesives, which were progressively replaced during the 20th century by mixtures of natural resins or balsams, thanks to the increasing awareness of the deleterious effects induced by wax and glue paste to the paint layer, such as darkening and shrinkage, respectively. Throughout the 1970s and 1980s, new synthetic adhesives such as BEVA371 and Plextol B500 were developed to improve the reversibility and stability of the lining process. In the present case, BEVA371 was used for the lining. The foresaid painting had undergone the lining operation due to a cut. Nearby the cut, the paint layer was reconstructed with a pictorial retouching, which is hardly distinguishable from the original paint.

Figure 63: Photo of the painting (Visible).

The analyzed painting was a challenging case for the testing of the performance of the PAI system, since the presence of the double canvas is expected to attenuate the intensity of PA waves propagating throughout the material, hindering the detection of the ultrasounds and, therefore, the visualization of hidden features. Thus, the efficiency of the system could be superior if the examined painting has a single canvas, which is the most common case.

The images acquired with the PAI system were ranging from $3x3cm^2$ to $4x4^2$ and the pixel dimension was kept constant and equal to 400μm. Furthermore, in order to increase the SNR, 6 waveforms were averaged for the acquisition of one PA signal.

After scanning the entire area of interest, the images were stitched together with the help of MosaicJ, an ImageJ plugin. What is more, the contrast of the images was enhanced. The PA imaging revealed a number of details about the restored area, some of which were not visible to the multispectral images. The findings were interpreted based on information provided by a restorer responsible for the most recent restoration of the painting. To begin with, the possible location of the cut in the historical canvas could be identified (the brighter 7-shaped region in the darker retouched area in Fig 64). As reported by the restorer, this interruption in the fabric was fixed by attaching the cut edges with an adhesive and then covered with a mixture of gypsum and animal glue to re-establish the continuity with the surrounding preparation layer. The detection of high-intensity PA signals in correspondence of this region is most probably due to the significant absorption of the NIR excitation radiation. On the contrary, the area of the retouching surrounding the cut produced weak

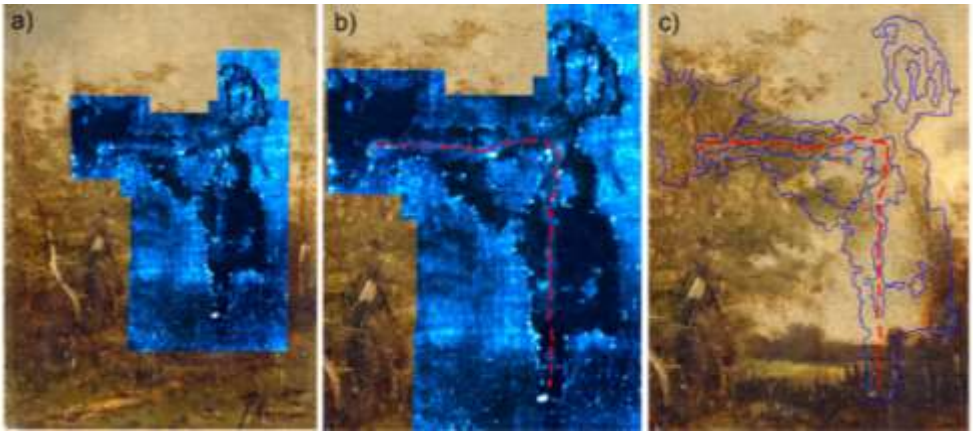

Figure 64: PAI analysis of the painting. a) PA image registered on the RGB image b) magnification of the PA image showing the shape of the retouching and the possible location of the 7-shaped cut, highlighted by the dashed red line c) outline of the retouching area revealed by the PAI (blue line).

PA signals, thus appearing darker in the PA image. According to the information provided by the conservator, the retouching was realized with a commercial tempera-paint (™Maimeri), which was then refined with a superimposed varnish-based paint. The PA image allows to clearly recognize the edges of the modern paint and to distinguish them from the leftover historical paint, corresponding to the light-blue portions inside the retouched area. The amplitude of the PA signal detected in these regions was indeed comparable to that measured in the area around the retouching, i.e. the aged paint.

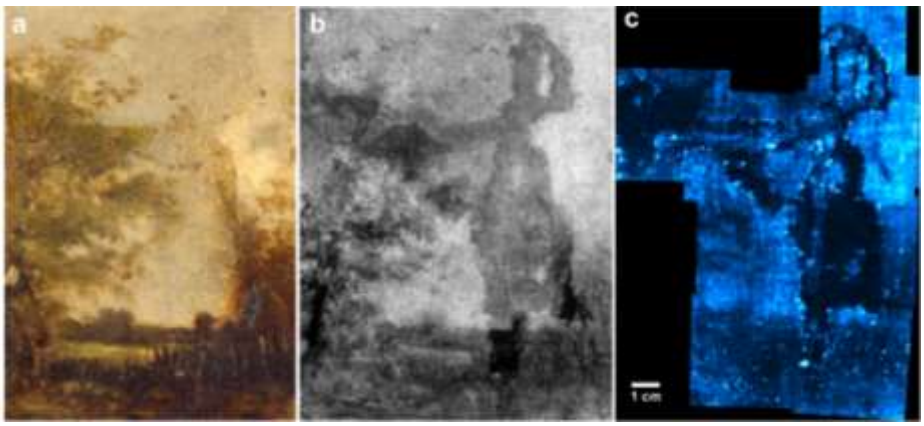

Figure 65: Different mages of the area of interest of the painting. a) RGB image b) NIR at 1940nm where the area of the retouching is visible (dark gray shape) c) PA image.

In Fig. 65, images acquired at different regions of the spectrum as well as the PA image are presented. The image shown in Fig. 65b was selected from the rest of the MSI photos, since it presented the highest contrast between the aged paint and the retouching area. The photo was obtained at 1940nm. It is evident that the PAI reveals the outline of the retouched area with greater detail and also, that the contrast of Fig. 65c (PAI) is greater than the one of Fig 65b.

The results of the case study were very fruitful, especially considering the fact that the sample did not have the ideal specifications for the needs of the testing of the PAI technique. A lot of information was obtained from the acquired images. The former proved that the PAI could be used additionally to the traditionally used methods with a view to better conserve cultural heritage items.

5.5.2. Visualization of paint cracks

In this final section of the results, is presented an early, yet really promising result of another PAI application, the detection of paint cracks in paintings. In Fig. 66a the mock-up painting is shown. The area of interest is marked with a red dashed rectangle, located near the bottom left side. The area of interest paint consists of consecutive Cobalt Blue (Winsor & Newton, Artists' Oil Colour, Cobalt Blue Deep 180 -Cobalt zinc silicate PB74) paint layers. The sample was left to age for some years and as a result, a number of cracks were created on its surface. The cracks are not visible with a naked eye (Fig. 66b) unless the sample is

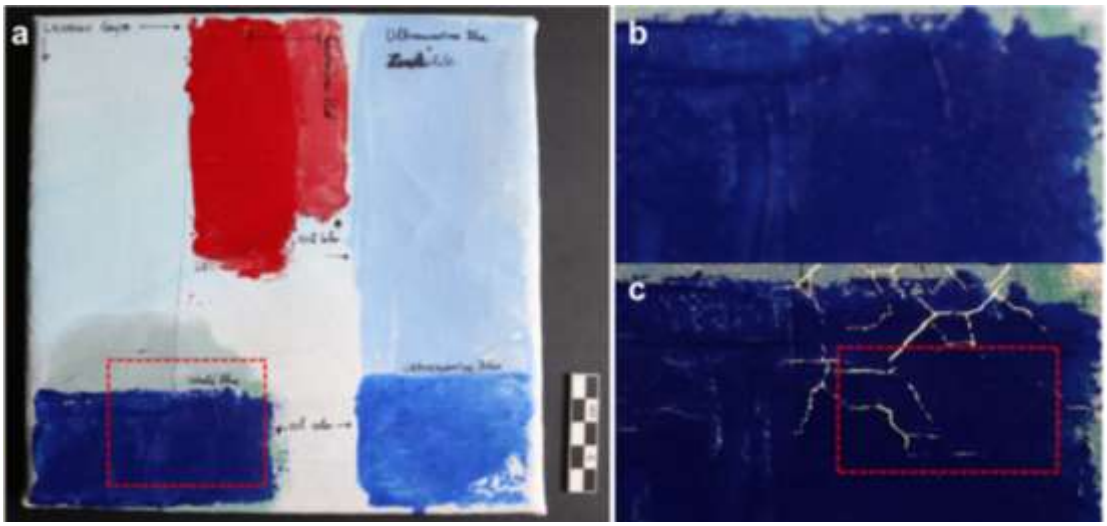

Figure 66: a) View of the mock-up painting. The area of interest is pointed out by a dashed rectangle b) magnification of the previous photo, showing the area of interest under regular lighting c) photo of the area of interest during the illumination of its rear side. The red dashed rectangle contains the area that was measured.

illuminated with a light source from its rear side. During the illumination, the cracks appear as seen in Fig. 66c. The PAI depicted the paint cracks with great accuracy as seen in Fig. 67. The positions of the cracks correspond to high PA signals, while the paint layer presents a very low, homogeneous, background signal. What is more, in the background the texture of the canvas can be observed. The reason why the PA signal is so intense in the case of the paint cracks is not obvious. The most probable explanation is that these high signals are

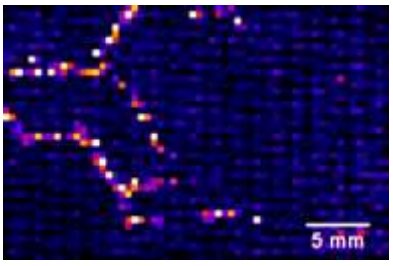

Figure 67: PA image of the area of interest.

produced at the edge of the paint (directly before and after each paint crack), since it has been observed that signals with high amplitudes are produced at the boundaries of samples of different materials.

6. Discussion

The PA phenomenon has found its place in cultural heritage conservation over the last years. It is apparent that it can prevail over other imaging techniques that face limitations due to lacking illumination. In the case of PAI, even if a small amount of light manages to reach the absorber (namely, the graphite, charcoal or any other material used to create the underdrawing), the ultrasound that is produced manages to traverse the distance between the absorber and the transducer without significant attenuation, and provide useful insight. On the contrary, in the existing optical techniques, the amount of light that reaches the area of interest has to travel through the sample twice in order to transfer the information, and that causes the intensity of the light that finally reaches the photodetector to decrease significantly, since its intensity is decreasing exponentially, as it has been previously mentioned (Beer-Lambert's law).

During the execution of this project, a number of important enhancements of the preexisting apparatus took place, which made the original set-up to seem very primitive. To begin with, the market research that led to the purchase of a water-immersion transducer sensitive to frequencies very close to those created due to the PA effect by the tested materials, increased both the quality and the SNR of the created images. Furthermore, the replacement of the motorized stages led to the increase of the system's capability concerning the scanning of artworks with larger dimensions. Additionally, the rewriting of the existing scripts responsible for the stages movement and the synchronization between the incidence of each pulse with the acquisition of the signals and the movement of the sample led to the attainment of the continuous scanning of the samples. This enhancement decreased dramatically the time needed for the acquisition of a PA image. What is more, during the realization of the project, we assessed the performance of agar gel in terms of signal propagation and detection properties, as well as in terms of non-invasiveness towards the delicate surfaces of fresco and secco wall paintings. When comparing to previously used media, i.e., distilled water, the use of agar proved to provide a comparable image contrast, at the same time acting as a surface protectant during the non-invasive examination of underdrawings and hidden features. The proposed methodological advancement, based on the use of agar gel as a new PA coupling medium, significantly broadens the applicability of the technique in the heritage science field.

There are, nevertheless some drawbacks and disadvantages to the technique. To begin with, the acquisition of the PA waves is presently accomplished with the use of a water-immersion transducer. This excludes the description of the method as "non-contact", and could discourage some heritage experts from using it on artworks of great cultural significance. What is more, the use of a water-immersion transducer creates an additional, practical issue, which is the submergence of a mural into the water. There are, though, purpose-built ultrasonic gels that have the same refractive index -and optical properties- with water and

thus, they could replace it in order to facilitate the measurements done on vertical surfaces. One of the foresaid gels was the one used for the needs of this work (namely agarose). The results of the comparison were very promising towards the replacement of water with agarose gels as the coupling medium. Nevertheless, the most important step towards the enhancement of the technique is the use of air-coupled transducers, as non-contact methods in cultural heritage diagnostics is a huge prerogative. What is more, the time needed for the scanning of a relatively small surface (~10cm^2) with the aforementioned experimental apparatus, lasts approximately 75mins. The aim of the project is to locate and reconstruct underdrawings of murals, which means that the scanning will have to cover a surface with a relative size of a few m^2. Thus, the further decrease of the time needed for the scan of a sample is necessary to take place. A step towards the augmentation of the speed is the use of a laser with shorter pulse duration. Another approach could be the use of galvo-mirrors that scan the specimen more rapidly.

In this paragraph some of the potential enhancements of the system are presented. To begin with, supplementarily to the detection of the ultrasounds due to the PA effect, with the use of the pulse-echo function of an ultrasonic transducer –which is based on the inverse piezoelectric effect–, we could collect information about the morphology of the surface of the scanned area as well. The inverse piezoelectric effect occurs when a wave pressure is created due to the influence of an electric field over a piezoelectric crystal. This wave pressure reaches the upper surface of the sample and after its reflection it can be detected by the transducer. What is more, in order to achieve greater penetration of the incident light into the mural, wavefront shaping techniques could replace the simple, focused irradiation of the specimens, appropriately preparing the incident light for the interaction with the surface of the sample. Furthermore, a multispectral PA excitation approach combined with suitable spectral unmixing algorithms could enable a high sensitivity differentiation of absorbers presenting comparable absorption. Multispectral PA excitation denotes that the light source used for the excitation of the absorber has a number of different wavelengths, in order to be capable of producing signals from absorbers with different chemical composition, which absorb radiation at different wavelengths. In the same direction, an analysis in the frequency domain could provide additional information compared to the time domain.

7. Summary

During the elaboration of the current study, the enhancement of an innovative, non-destructive, detection technique for mural underdrawings was realised, based on the principles of PA microscopy. The imaging method is based on the absorption of IR radiation by the material used for the underdrawing, which leads to the creation of a wave pressure. This wave pressure results in the creation of an ultrasound, which is detected by an ultrasonic transducer. The waveform is saved in binary form to a computer with a view to creating the PA image, or the stratigraphic profile of the sample. The results of the experiments are very promising and the technique has demonstrated the excellent capabilities of PAI to uncover hidden content in mural samples consisting of different pigments, or even, a combination of paint and gypsum. Lastly, the fact that the specific

technique is relatively low-cost and it does not require a very sophisticated or complex configuration should be reported. We hope that with proper modifications and enhancements, this experimental set-up could become a useful tool for art conservators and restorers.

8. References

[1] Tserevelakis, G. J., Vrouvaki, I., Siozos, P., Melessanaki, K., Hatzigiannakis, K., Fotakis, C., & Zacharakis, G. (2017). *Photoacoustic imaging reveals hidden underdrawings in paintings. Scientific Reports, 7(1).* doi:10.1038/s41598-017-00873-7

[2] Tserevelakis, G. J., Dal Fovo, A., Melessanaki, K., Fontana, R., & Zacharakis, G. (2018). *Photoacoustic signal attenuation analysis for the assessment of thin layers thickness in paintings. Journal of Applied Physics, 123(12).* doi:10.1063/1.5022749

[3] Tserevelakis, G. J., Tsagkaraki, M., Siozos, P., & Zacharakis, G. (2018). *Uncovering the hidden content of layered documents by means of photoacoustic imaging. Strain, e12289.* doi:10.1111/str.12289

[4] Tserevelakis, G. J., Tsafas V., Melessanaki, K., Zacharakis, G. & Filippidis, G. (2019). *Combined multiphoton fluorescence microscopy and photoacoustic imaging for stratigraphic analysis of paintings. Optics Letters, 44(5).* doi:10.1364/OL.44.001154

[5] Tserevelakis, G. J., Siozos, P., Papanikolaou, A., Melessanaki, K., & Zacharakis, G. (2019). *Non-invasive photoacoustic detection of hidden underdrawings in paintings using air-coupled transducers. Ultrasonics.* doi:10.1016/j.ultras.2019.06.008

[6] Dal Fovo A., Tserevelakis G.J., Klironomou E., Zacharakis G., Fontana R. (2021). *First combined application of photoacoustic and optical techniques to the study of an historical oil painting, European Physics Journal Plus 136.* doi:10.1140/epjp/s13360-021-01739-8

[7] Tserevelakis G.J., Chaban A., Klironomou E., Melessanaki K., Striova J., Zacharakis G. (2021). *Revealing Hidden Features in Multilayered Artworks by Means of an Epi-Illumination Photoacoustic Imaging System, Journal of Imaging, 7(9).* doi:10.3390/jimaging7090183

[8] Chaban A., Tserevelakis G.J., Klironomou E., Fontana R., Zacharakis G., Striova J. (2021). Revealing Underdrawings in Wall Paintings of Complex Stratigraphy with a Novel Reflectance Photoacoustic Imaging Prototype, *Journal of Imaging, 7(12)*. doi:10.3390/jimaging7120250

[9] Chaban A., Tserevelakis G.J., Klironomou E., Zacharakis G., Striova J. (2022) *Agar gel as non-invasive coupling medium for reflectance photoacoustic (PA) imaging: first experimental results on wall painting mock-ups Journal of Imaging, 8(9), 235.* doi:10.3390/jimaging8090235

[10] Pisu, F.A., Chiriu, D., Klironomou, E., Zacharakis, G., Tserevelakis, G.J. (2023) *Stratigraphy of Fresco Paintings: A New Approach with Photoacoustic and SORS Imaging. J. Imaging 2023, 9(1), 16*. doi:10.3390/jimaging9010016

[11] Zhang, Yi, *Measuring Acoustic Attenuation of Polymer Materials Using Drop Ball Test* (2013). *Dissertations and Theses*. 151.

[12] Wang, L. V., & Wu, H. (2007). *Biomedical optics principles and imaging*. Somerset, NJ, USA: Wiley.

[13] Jackson, J. B., Mourou, M. R., Whitaker, J. F., Duling, I. N., Williamson, S. L., Menu, M., & Mourou, G. A. (2008). *Terahertz time-domain reflectometry applied to the investigation of hidden mural paintings. 2008 Conference on Lasers and Electro-Optics.* doi:10.1109/cleo.2008.4551489

[14] Heitzmann, R. (2006). *Band Limit and Appropriate Sampling in Microscopy*, Chapter 3, p. 29-36 in: Cell Biology

[15] Turner, N., Patterson, C., MacLennan, D. and Trentelman, K.(2018). *Visualizing underdrawings in medieval manuscript illuminations with macro-X-ray fluorescence scanning. X-Ray Spectrometry, 48(4), pp.251-261.* doi:10.1002/xrs.2956

[16] Gettens, R. J., & Stout, G. L. (1947). *Painting Materials: A Short Encyclopedia* (4th ed.). Dover Publications.

[17] Yao, J., & Wang, L. V. (2013). *Photoacoustic microscopy. Laser & Photonics Reviews, 7(5), 758–778.* doi:10.1002/lpor.201200060

[18] Azhari, H., 2010. *Basics of Biomedical Ultrasound for Engineers*. Wiley. Chapter 9, p. 195-196

[19] Daniilia, S., Tsakalof, A., Bairachtari, K., & Chryssoulakis, Y. (2007). *The Byzantine wall paintings from the Protaton Church on Mount Athos, Greece: tradition and science. Journal of Archaeological Science, 34(12), 1971–1984.* doi:10.1016/j.jas.2007.01.016

[20] Thompson, D. V. (1956). *The Materials and Techniques of Medieval Painting (Dover Art Instruction). Dover Publications.*

[21] Bendada, A., Sfarra, S., Ibarra−Castanedo, C., Akhloufi, M., Caumes, J. P., Pradere, C., Batsale, J. C., Maldague, X. (2015). *Subsurface imaging for panel paintings inspection: A comparative study of the ultraviolet, the visible, the infrared and the terahertz spectra. Opto-Electronics Review, 23(1).* doi:10.1515/oere-2015-0013

[22] Van Asperen de Boer, J. (1975). An introduction to the scientific examination of paintings. *Nederlands Kunsthistorisch Jaarboek (NKJ) / Netherlands Yearbook for History of Art, 26*, 1-40.

[23] Van Asperen de Boer, J. R. J. (1968). *Infrared Reflectography: a Method for the Examination of Paintings. Applied Optics, 7(9), 1711.* doi:10.1364/ao.7.001711

[24] Βεληβασάκη, Μ., Διπλωματική εργασία, Ηράκλειο 2016

[25] Βρουβάκη, Η., Διπλωματική εργασία, Ηράκλειο 2016

[26] White, R. M. (1963). *Generation of Elastic Waves by Transient Surface Heating. Journal of Applied Physics, 34(12), 3559–3567.* doi:10.1063/1.1729258

[27] Brienza, M. J., & DeMaria, A. J. (1967). *LASER-INDUCED MICROWAVE SOUND BY SURFACE HEATING. Applied Physics Letters, 11(2), 44–46.* doi:10.1063/1.1755021
[28] Von Gutfeld, R. J., & Melcher, R. L. (1977). *20-MHz acoustic waves from pulsed thermoelastic expansions of constrained surfaces. Applied Physics Letters, 30(6), 257–259.* doi:10.1063/1.89375

[29] Wickramasinghe, H. K., Bray, R. C., Jipson, V., Quate, C. F., & Salcedo, J. R. (1978). *Photoacoustics on a microscopic scale. Applied Physics Letters, 33(11), 923–925.* doi:10.1063/1.90219

[30] Fukunaga, K., Picollo, M. (2010). *Terahertz spectroscopy applied to the analysis of artists' materials. Applied Physics A, 100(3), 591–597.* doi:10.1007/s00339-010-5643-y

[31] Adam, A. J. L., Planken, P. C. M., Meloni, S., & Dik, J. (2009). *TeraHertz imaging of hidden paint layers on canvas. Optics Express, 17(5), 3407.* doi:10.1364/oe.17.003407

[32] Filippidis, G., Massaouti, M., Selimis, A., Gualda, E. J., Manceau, J.-M., & Tzortzakis, S. (2011). *Nonlinear imaging and THz diagnostic tools in the service of Cultural Heritage. Applied Physics A, 106(2), 257–263.* doi:10.1007/s00339-011-6691-7

[33] Faries, M., Defoer, H. "Jan van Scorel's *Crucifixion* for the Oude Kerk, Amsterdam: The "finest painting in all of the regions of Flanders"," *Journal of Historians of Netherlandish Art* 12:2. doi:10.5092/jhna.2020.12.2.1

[34] Filedt Kok, J. P. (1978). *Underdrawing and other technical aspects in the paintings of Lucas van Leyden. Netherlands Yearbook for History of Art / Nederlands Kunsthistorisch Jaarboek, 29(1), 1–184.* doi:10.1163/22145966-90000496

[35] Syson, L., & Billinge, R. (2005). *Leonardo da Vinci's Use of Underdrawing in the 'Virgin of the Rocks' in the National Gallery and 'St. Jerome' in the Vatican*. *The Burlington Magazine, 147*(1228), *450-463.*

[36] Liang, H. (2011). *Advances in multispectral and hyperspectral imaging for archaeology and art conservation. Applied Physics A, 106(2), 309–323.* doi:10.1007/s00339-011-6689-1

[37] Dik, J., Janssens, K., Van Der Snickt, G., van der Loeff, L., Rickers, K., & Cotte, M. (2008). *Visualization of a Lost Painting by Vincent van Gogh Using Synchrotron Radiation Based X-ray Fluorescence Elemental Mapping. Analytical Chemistry, 80(16), 6436–6442.* doi:10.1021/ac800965g

[38] Adler, D. C., Stenger, J., Gorczynska, I., Lie, H., Hensick, T., Spronk, R., Wolohojian, S., Khandekar, N., Jiang, J. Y., Barry, S., Cable, A. E., Huber, R., Fujimoto, J. G. (2007). *Comparison of three-dimensional optical coherence tomography and high resolution photography for art conservation studies. Optics Express, 15(24), 15972.* doi:10.1364/oe.15.015972

[39] Faries, M. (1975). *Underdrawings in the workshop production of Jan van Scorel – A study with infrared reflectography. Nederlands Kunsthistorisch Jaarboek (NKJ) / Netherlands Yearbook for History of Art, Vol. 26, Scientific examination of early Netherlandish Painting: Applications in art history, pp. 89-228*

[40] Hain, M.; Bartl, J.; Jacko, V. (2003). *Multispectral analysis of cultural heritage artefacts. Measurement of Physical Quantities, 3, 9-12*

[41] Daukantas, P. (2018). *Cultural Artifacts in Terahertz Light. Optics and Photonics News, 29(3), 28.* doi:10.1364/opn.29.3.000028

[42] Oshana, R. (2006). *Overview of Digital Signal Processing Algorithms. DSP Software Development Techniques for Embedded and Real-Time Systems, 59–121.* doi:10.1016/b978-075067759-2/50006-5

[43] SILVERMAN, R. H., VINARSKY, E., WOODS, S. M., LIZZI, F. L., & COLEMAN, D. J. (1995). *THE EFFECT OF TRANSDUCER BANDWIDTH ON ULTRASONIC IMAGE CHARACTERISTICS. Retina, 15(1), 37–42.* doi:10.1097/00006982-199515010-00008

[44] https://www.bio-rad.com/featured/en/agarose.html